COMPARATIVE STUDIES OF
ASTROPHYSICAL GAMMA-RAY EVENTS
DETECTED WITH *FERMI*/GBM

by
ÖZGE KESKİN

Submitted to the Graduate School of Engineering and Natural Sciences
in partial fulfillment of the requirements for the degree of
Master of Science

Sabancı University
July 2021

COMPARATIVE STUDIES OF
ASTROPHYSICAL GAMMA-RAY EVENTS
DETECTED WITH *FERMI*/GBM

Approved by:

Date of Approval: July 6, 2021

ACKNOWLEDGEMENTS

To my sisters

ABSTRACT

COMPARATIVE STUDIES OF ASTROPHYSICAL GAMMA-RAY EVENTS
DETECTED WITH *FERMI*/GBM

ÖZGE KESKİN
PHYSICS, M.SC. THESIS, July 2021

Thesis Advisor: Prof. Dr. Ersin Göğüş
Thesis Co-Advisor: Assoc. Prof. Dr. Yuki Kaneko

Keywords: Gamma-ray Transient Sources, Astronomical Object Identification

The aim of this study is to define well-constrained parameters for classification of gamma-ray transient events found in comprehensive untriggered-event searches. To this end, we studied the triggered events detected with Gamma-ray Burst Monitor (GBM) and classified by the Flight Software (FSW) on the *Fermi* Gamma-ray Space Telescope. The main classifications of gamma-ray events in *Fermi*/GBM Trigger Catalog are gamma-ray bursts (GRB), soft gamma repeaters (SGR), terrestrial gamma-ray flashes (TGF), solar flares (SFL), transients (TRANSNT), and charged-particle events. In this thesis, we present a comparative study of these events, based on which we suggest possible classification methods and demonstrate how this study will be used to classify untriggered GBM events.

We first performed duration and hardness analysis to identify characteristic properties of event types. The durations of all triggered events were calculated via Bayesian Block method, and the duration distribution of each class was obtained. Then, all burst types were divided into two categories as short ($\lesssim$ 2 s ; SGRB, SGR, TGF) and long ($\gtrsim$ 2 s ; LGRB, SFL, TRANSNT) events based on the results. For further classification, we calculated spectral hardness in the energy range of 10-2000 keV. The least overlap in the hardness distributions of different event classes was obtained when we used 50 keV and 75 keV as breaking (pivot) points between the soft and hard energy bands for short and long lasting events, respectively. We additionally developed an algorithm to differentiate transient bursts from pulsations and Earth occultations of known astrophysical sources, all of which are classified as transients in the *Fermi*/GBM Trigger Catalog. Moreover, we differentiated particle events with the help of the McIlwain L coordinate of the spacecraft and maximum to minimum ratio of the count rates of the 12 sodium iodide (NaI(Tl)) detectors in the energy range of 50-300 keV at the time of the trigger.

ÖZ

FERMİ/GBM TETİKLEMİŞ ASTROFİZİKSEL GAMA IŞINI OLAYLARININ KARŞILAŞTIRMALI ÇALIŞMASI

ÖZGE KESKİN
FİZİK, YÜKSEK LİSANS TEZİ, Temmuz 2021

Tez Danışmanı: Prof. Dr. Ersin Göğüş
Eş Tez Danışmanı: Doç. Dr. Yuki Kaneko

Anahtar Kelimeler: Geçici Gama Işını Kaynakları, Astronomik Cisim Tanımlama

Bu çalışmanın amacı, kapsamlı tetiklememiş olay araştırmalarında bulunan geçici gama ışını olaylarının sınıflandırılması için iyi kısıtlanmış parametreler tanımlamaktır. Bu amaçla, *Fermi* Gama Işını Uzay Teleskobu üzerinde bulunan GBM ile tespit edilmiş ve FSW tarafından sınıflandırılmış tetiklemiş olaylar üzerine çalıştık. *Fermi*/GBM Tetiklemiş Kataloğundaki gama ışını olaylarının başlıca sınıflandırmaları şunlardır: gama ışını patlamaları (GRB), tekrarlayan yumuşak gama ışını kaynakları (SGR), karasal gama ışını parlamaları (TGF), güneş patlamaları (SFL), geçici olaylar (TRANSNT) ve yüklü parçacık olayları. Bu tezde, olası sınıflandırma yöntemlerini önerdiğimiz bu olayların karşılaştırmalı bir çalışmasını sunuyor ve tetiklememiş GBM olaylarının bu çalışma ile nasıl sınıflandırılabileceğini gösteriyoruz.

Öncelikle olay türlerinin karakteristik özelliklerini belirlemek için süre ve sertlik analizleri uyguladık. Tüm tetiklemiş olayların sürelerini Bayesian Blok yöntemi ile hesapladıktan sonra her bir sınıfın süre dağılımını elde ettik. Bu süre sonuçlarını baz alarak bütün olay türlerini kısa ($\lesssim$ 2 s ; SGRB, SGR, TGF) ve uzun ($\gtrsim$ 2 s ; LGRB, SFL, TRANSNT) olaylar olmak üzere iki kategoriye ayırdık. Daha ileri sınıflandırma için 10-2000 keV enerji bandında spektral sertlik hesaplamaları yaptık. Farklı sınıfların sertlik dağılımlarında en az örtüşmeyi, yumuşak ve sert enerji bandı arasındaki kırılma (pivot) noktasını kısa ve uzun olaylar için sırasıyla 50 ve 75 keV olarak aldığımızda elde ettik. Ek olarak, *Fermi*/GBM tetiklemiş kataloğunda hepsi geçici olaylar olarak sınıflandırılan, bilinen astrofiziksel kaynakların atmalarından ve Dünya örtülmelerinden geçici patlamaları ayırt etmek için bir algoritma geliştirdik. Ayrıca, tetikleme zamanında uzay aracının McIlwain L koordinatı ve 50-300 keV enerji bandında 12 dedektördeki foton seviyesinin maksimumun minimuma oranı yardımıyla yüklü parçacık olaylarını ayrıştırdık.

TABLE OF CONTENTS

LIST OF TABLES

LIST OF FIGURES

LIST OF ABBREVIATIONS

BB: Bayesian Block . . . .

BGO: Bismuth Germanate Scintillation Detector . . . .

CTTE: Continuous Time-Tagged Event . . . .

DISTPAR: Distant Particle Event . . . .

FERMI: *Fermi* Gamma-Ray Space Telescope . . . .

FERMIGTRIG: *Fermi*/GBM Trigger Catalog . . . .

FOV: Field of View . . . .

FSW: Flight Software . . . .

GBM: Gamma-Ray Burst Monitor . . . .

GRB: Gamma-Ray Burst . . . .

HR: Hardness Ratio . . . .

LAT: Large Area Telescope . . . .

LGRB: Long GRB . . . .

LOCLPAR: Local Particle Event . . . .

L-SHELL: McIlwain L Coordinate . . . .

NaI(T1): Thallium Activated Sodium Iodide Scintillation Detectors . . . .

SAA: South Atlantic Anomaly . . . .

SFL: Solar Flare . . . .

SGR: Soft Gamma Repeater . . . .

SGRB: Short GRB . . . .

TGF: Terrestrial Gamma-Ray Flash . . . .

TRANSNT: Transient Event . . . .

TTE: Time-Tagged Event . . . .

1 INTRODUCTION

The *Fermi* Gamma-ray Space Telescope *(Fermi)* has been operating successfully since its launch in 2008 and providing an enormous amount of data to study various types of gamma-ray transient events such as gamma-ray bursts, solar flares, terrestrial gamma-ray flashes, and soft gamma repeaters. Hence, differentiation and classification of these events play a major role to benefit from this extensive data. The Gamma-ray Burst Monitor Flight Software (GBM FSW) on board *Fermi* performs an automatic event classification for triggered events by using a Bayesian probabilistic approach, comparing the observed properties of triggered events and expected properties of different classes. While doing the Bayesian analysis, the GBM FSW takes into account: the event localization, including distance from the sun and other known sources; spectral hardness, counts in 50-300 keV/10-50 keV; and the spacecraft geomagnetic latitude, McIlwain L coordinate (Meegan et al. 2009).

This study aims to extend that classification scheme to classify untriggered, unclassified events found in untriggered-event searches. To this end, we present a comparative study of gamma-ray transient events, based on which we suggest possible classification methods and demonstrate how these methods will be used to classify untriggered GBM events.

In this thesis, an introduction to *Fermi*/GBM is found in Section 1.1, event types which trigger the GBM are explained in Section 1.2, and the statistical analysis of these triggered events is presented in Section 1.3. In Section 2, how duration and hardness analyses of the triggers are performed and the classification and identification methods used are shown. In Section 3, the results are presented and discussed. Finally, a summary is presented and future prospects are expanded in Section 4.

1.1 *Fermi*/GBM

The *Fermi* Gamma-ray Space Telescope[1] (formerly, the Gamma-ray Large Area Space Telescope), launched on June 11, 2008 into a low Earth orbit (565 km) with an inclination of 25.6 degree, is a space observatory designed to study gamma-ray sources (Gruber et al. 2014). It carries two science instruments: the Large Area Telescope (LAT ; Atwood et al.

---

[1]The *Fermi* Gamma-ray Space Telescope: https://fermi.gsfc.nasa.gov/.

2009) which observes gamma-rays from ~ 20 MeV to ~ 300 GeV and the Gamma-ray Burst Monitor (GBM ; Meegan et al. 2009) which makes observations at energies in the range from ~ 8 keV to ~ 40 MeV, and thus provides a broadband (over seven decades in energy) spectral information of a wide range of astronomical sources (Bhat et al. 2016).

The primary objective of GBM is to detect and locate Gamma-ray Bursts (GRBs), and it has a wide field of view (FOV: 8sr ; un-occulted by Earth). The GBM consists of twelve thallium-activated sodium iodide (NaI(Tl)) scintillation detectors in the energy range from ~ 8 keV to ~ 2 MeV and two bismuth germanate (BGO) scintillation detectors in the energy range from ~ 200 keV to ~ 40 MeV. The NaI(Tl) detectors are positioned as four groups of 3 each (see Figure 1) to acquire the whole sky FOV, and by using the relative count rates of these detectors, GBM roughly computes locations of triggered events and allows the immediate reorientation of spacecraft to enable LAT to observe possible delayed hard-energy emission of bright bursts. On the other hand, the BGO detectors are placed at the opposite sides of the spacecraft so that at least one of them can detect an event if it occurs above the horizon. Moreover, BGO detectors provide cross calibration between the two experiments since they overlap with NaI(TI) detectors at low energy ranges and with LAT at high energy ranges.

There are three types of continuously-accumulated GBM data: CTIME data with high time resolution (nominally 256 ms) and low energy resolution (8 channels); CSPEC data with low time resolution (nominally 4096 ms) and high energy resolution (128 channels); and CTTE (Continuous Time-Tagged Event) data with a resolution of 2 μs and 128 energy channels, which became available after July 16, 2010.

The GBM instrument is triggered if the FSW detects an increase in the count rates of two or more NaI(Tl) detectors exceeding a threshold value. This threshold is an adjustable value determined in units of the standard deviation of the background rate, which is an average of the accumulated count rates over the previous 17 seconds, excluding four seconds close to the trigger time (Meegan et al. 2009). When a trigger occurs, the FSW changes the data output by increasing time resolutions of CTIME and CSPEC data from the above-mentioned nominal values to 64 ms and 1024 ms, respectively, during nominally 600 seconds after trigger and also generates nominally 330 seconds of TTE data, starting 30 seconds before the trigger time.

Detailed information of all GBM triggers are accessible through the *Fermi*/GBM Trigger Catalog[2] (FERMIGTRIG), which is a browsable trigger catalog accessible online at

---

[2]The *Fermi*/GBM Trigger Catalog: https://heasarc.gsfc.nasa.gov/FTP/fermi/data/tdat/heasarc-fermigtrig.tdat.

High Energy Astrophysics Science Archive Research Center (HEASARC) and consists of trigger name, trigger time, triggered detectors, trigger algorithm number, and localization and classification of the trigger with the probability of classification. The FERMIGTRIG is a dynamic catalog and automatically updated as new triggers are identified.

Finally, we note that the detectors of GBM are shut down during the spacecraft's transit through the South Atlantic Anomaly (SAA), a region where the inner Van Allen radiation belt comes closer to the Earth surface and exposes *Fermi* to intense radiation and high particle activity, thus count rates of the detectors goes to zero in this region. While passing the SAA boundaries, however, the detectors monitor high rates and can cause a false trigger.
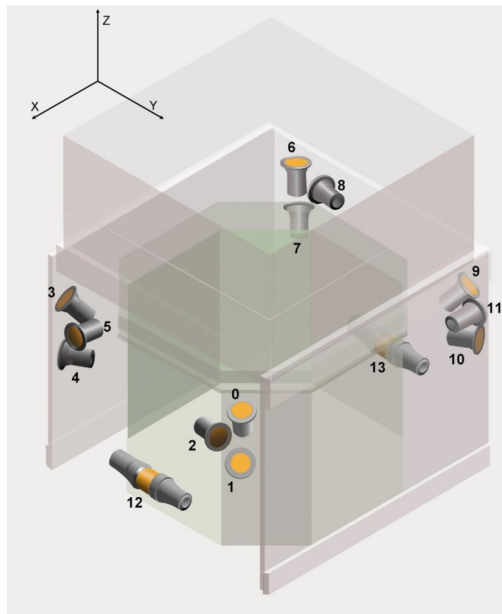
Figure 1 The locations and orientations of *Fermi*/GBM detectors. The 12 NaI(TI) detectors (0-11) and the BGO (12-13) are numbered. (Meegan et al. 2009)

1.2 *Fermi*/GBM Triggered Events

Besides GRBs, events that trigger the *Fermi*/GBM can be classified into six categories: Soft Gamma Repeaters (SGR), Solar Flares (SFL), Terrestrial Gamma-ray Flashes (TGF), Transients (TRANSNT), Local Particles (LOCLPAR), and Distant Particles (DISTPAR). This section is devoted to a brief description of each class.

GRBs are intense and non-repeating gamma-ray transient events that lead to the formation of compact stars, mostly black holes. They are usually further classified into two

classes, short-hard GRBs and long-soft GRBs (Kouveliotou et al. 1993), based on their durations and spectral hardnesses, and differ by the nature of their progenitors. Short GRB events (SGRBs) have durations of less than ~ 2 seconds, and they are related to the mergers of two compact objects such as black hole-neutron star binaries and double neutron star binaries (Mochkovitch, Hernanz, Isern & Martin 1993 ; Eichler et al. 1989 ; Narayan, Paczynski & Piran 1992) in early type or star-forming galaxies (Bloom et al. 2006 ; Fong et al. 2013). Such mergers occur due to angular momentum and energy losses to the gravitational wave radiation, and there are two possible post-merger scenarios (Nakar 2007): a black hole with an accretion disk enabling the SGRB and its afterglow or a magnetar (Rowlinson et al. 2013 ; Zhang 2013). Long GRB events (LGRBs), however, last longer than ~ 2seconds and are likely to be associated with massive stars collapsing into black holes (Woosley 1993) or neutron stars (Thompson, Chang & Quataert 2004) with Type 1c core-collapse supernovae (Woosley & Bloom 2006) ; MacFadyen, Woosley & Heger 2001) in late-type star-forming galaxies (Bloom, Kulkarni & Djorgovski 2002 ; Wainwright, Berger & Penprase 2007).

SGRs, currently known as magnetars, are young($\sim 10^3$ years old), slowly rotating (2-12 s) neutron stars associated with extreme magnetic fields (B $> 10^{14}$ G) (Kouveliotou et al. 1998 ; Göğüş et al. 2010). Magnetars' spatial distribution in the Galaxy is strictly confined to the Galactic plane, which means that they are galactic sources. Spontaneous decay of the enormous magnetic field provides an energy source for short bursts and long outbursts as well as persistent emission, especially in the x-ray and gamma-ray band (Duncan & Thompson 1992 ; Thompson & Duncan 1995 ; Thompson & Duncan 1996). The most common type of observed magnetar events is short bursts, with durations in the range from a few milliseconds to a few seconds (Göğüş et al. 2001) and energy release of over $\sim 10^{38}$ erg. In addition, short bursts tend to be single-peaked and decay slowly compared to the rise (Göğüş et al. 2001). There are two more types of SGR burst: giant flares and intermediate bursts. The giant flares are associated with catastrophic events involving an initial pulse with sudden release of over 10^{44} erg of energy followed by a tail which decays in long periods. They are spectrally harder, peaking in the soft gamma-ray band and extending at least to MeV energies (Kaspi & Beloborodov 2017). Only three giant flares have been observed to date. The intermediate events are between the short bursts and giant flares in terms of durations ranging from a few seconds to a few tens of seconds and energy release up to $\sim 10^{42}$ erg (Kozlova et al. 2016).

TGFs are ultra-intense submillisecond gamma-ray pulses (Briggs et al. 2013) and hence easily detectable at hundreds of kilometers above the Earth by *Fermi* and were discovered by the Burst and Transient Source Experiment on the *Compton Gamma Ray Space Observatory* (Fishman et al. 1994). They occur during intracloud lightning (Stan-

ley et al. 2006) due to acceleration of electrons by the relativistic runaway electron avalanche process (Gurevich et al. 1992). The relativistic electrons interact with nuclei of atoms in the atmosphere and produce gamma-rays via bremsstrahlung (Gehrels & Cannizzo 2012), so that TGFs attain hard energy spectra up to several tens of MeV (Briggs et al. 2010). TGFs generally last less than a millisecond, however, TGFs with long tails due to prolonged scattering in the atmosphere can be longer than a millisecond in duration (Roberts et al. 2018).

SFLs are large eruptions that occur near sunspots due to rapid energy release previously stored as inductive magnetic fields due to electrical currents flowing into the corona; their frequency of occurrence depends on the 11-year solar cycle. They can be quite energetic (in excess of 10^{32} erg of energy), releasing energy across the entire electromagnetic spectrum from radio waves to gamma-rays, and their durations can vary from seconds to hours (Fletcher et al. 2011).

TRANSNT classification depends on the definition of "transient" and on the sensitivity of the instrument. TRANSNTs in *Fermi*/GBM Trigger Catalog are defined as non-SGR bursting activity of Galactic sources by Von Kienlin et al. (2020). These sources can also go through gamma-ray outburst periods.

Particle events (LOCLPARs and DISTPARs) occur due to mostly charged particles of magnetospheric origin or occasionally cosmic ray showers. The charged particles trapped by the Earth's magnetic field in Van Allen Belts can initiate a trigger during the *Fermi*'s transit mostly in the entry or exit regions of SAA or at high geomagnetic latitude (Von Kienlin et al. 2020), and these events can be also called magnetic particle precipitation events. Cosmic ray showers may occur near or within the spacecraft and cause onboard triggers. Events that occur close to the spacecraft are called local particles. Such particle events are simultaneously detected by most of the GBM detectors and hence the light curves of 12 NaI(Tl) detectors are quite similar in the 50-300 keV range (Jenke et al. 2016). Distant particle events, however, occur around the Earth's horizon and hence can be seen by only a few detectors, unlike local particle events.

1.3 *Fermi*/GBM Trigger Statistics

The GBM instrument has been triggered 7477 times as of December 31, 2020, of which 2971 triggers are classified as **GRBs**, (i.e., average of ~ 238 GRBs per year). Table 1 presents the number of triggers for different event types.

Table 1 Annual Distribution of *Fermi*/GBM Triggered Events as of December 31, 2020

YEAR	GRB	SFL	SGR	TGF	TRANSNT	LOCLPAR	DISTPAR	OTHER	TOTAL
2008	124	1	14	8	0	2	0	11	160
2009	250	5	134	20	1	18	0	23	451
2010	242	31	2	102	1	47	7	31	463
2011	219	189	15	87	0	69	8	27	614
2012	220	215	3	105	0	54	8	40	645
2013	232	189	7	94	0	46	6	31	605
2014	242	296	3	113	2	27	4	31	718
2015	237	163	19	107	173	287	21	50	1057
2016	220	33	50	93	0	181	10	29	616
2017	251	53	5	96	190	185	11	45	836
2018	243	1	6	107	38	58	6	29	488
2019	231	5	15	77	8	20	1	29	386
2020	260	8	45	83	17	4	0	21	438
TOTAL	2971	1189	318	1092	430	998	82	397	7477

Note that the number of triggers in 2008 are less than the following years due to the *Fermi*'s launch in the half of 2008.

It is evident from Table 1 that for other types, the number of detections can vary significantly. For example, most of the **SGR** bursts took place in 2009. These bursts originated mainly from SGR J1550–5418 (Kaneko et al. 2010). Also, the last completed Solar cycle was in between 2008-2019, and the number of **SFLs** increased during the solar maximum period (2010-2017) and reached its maximum value in 2014, as clearly seen in Table 1.

Some of the detection number variations are due to the change in technical specifications. In case of **TGFs**, the number of detections increased from ~ 12 to ~ 97 per year thanks to the activation of new triggering algorithms that include BGO detectors in November 10, 2009 (Fishman et al. 2011). Since TGFs have hard energy spectra up to several tens of MeV, BGO detectors are more likely to detect them compared to NaI(Tl) detectors. Also, the number of particle events (**LOCLPARs** and **DISTPARs**) that triggered GBM rose in between 2015 and 2017. These are mainly in the boundaries of SAA and may stem from the expansion of predefined SAA borders stored in the GBM FSW (Von Kienlin et al. 2020).

Additionally, **TRANSNTs** triggered GBM numerous times in June 2015 and November 2017 as shown in the 'TRANSNT' column in Table 1. These triggers mainly stem from outbursts of two sources: V404 CYG (Jenke et al. 2016), a black hole binary transient, and Swift J0243.6+6124 (Wilson-Hodge et al. 2018), a binary transient with a first known galactic ultraluminous pulsar, respectively. The triggers due to these two sources are identified and included into 'Other' class in Figure 2. In addition to that, some triggers that are classified as TRANSNT are due to known astrophysical sources

6

that come out of Earth occultation and also included in 'Other' category in Figure 2. These processes are described in detail in Section 2.4. Finally, triggers with uncertain classification fall into the 'Other' section.
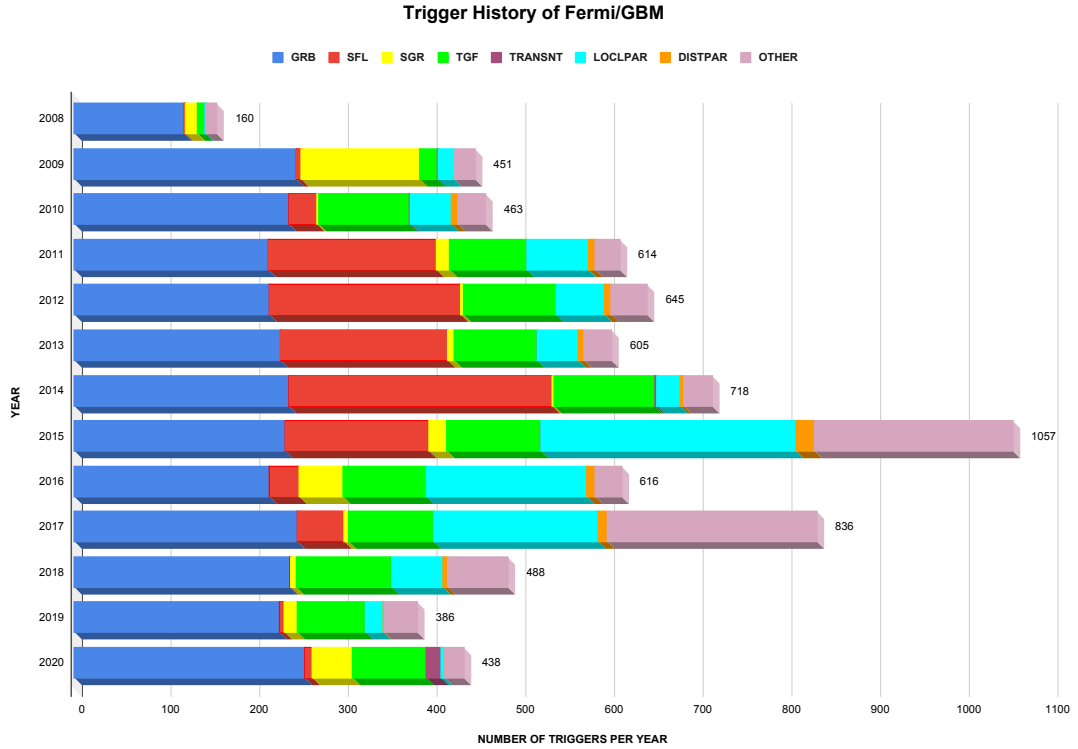
Figure 2 Trigger History of *Fermi*/GBM as of December 31, 2020

2 ANALYSIS METHODOLOGY

In order to identify characteristic properties between the triggered events from different classes, we first performed duration and hardness analysis. Moreover, we used the spacecraft's geomagnetic latitude (McIlwain L coordinate) and maximum-minimum ratio of the count rates of the 12 NaI(Tl) detectors to differentiate local particle events. Also, we developed an algorithm to distinguish pulsation and Earth occultation triggers of the known sources, which were excluded from the duration and spectral hardness calculation. We explain these in detail in this section.

2.1 Duration Analysis

We used the Bayesian Block Representation (BB ; Scargle et al. 2013) method to estimate the duration of each triggered event. This method is based on Bayesian analysis, which is used for the determination of the points of significant change in count rates of the light curve, hence the boundaries between the blocks. Therefore, the light curve is represented with a series of blocks, which does not have to be in the same sizes (bins). Bayesian Block technique is straightforward for duration calculation. First of all, it is appropriate for data with a broad range of time scales and noise levels. Also, it does not require any background subtraction. Thus, this method is a basic, simple, direct and objective method for duration calculation. Moreover, the Bayesian Block method provides the entire duration of the burst unlike T_{90} or T_{50} duration commonly used for GRBs and SGR bursts. T_{90} (T_{50}) burst duration is the interval between the times where the burst reached %5 (%25) and %95 (%75) of its total photon fluence (Bhat et al. 2016).

Table 2 Parameters in Duration Calculation for Each Class

CLASS	BKGTL(s)	TRES(ms)	TIME RANGE(s)^a	ENERGY RANGE(keV)	DATA
SGR	4.0	4	-10,10	10-100	TTE
TGF	0.5	1	-1,1	300-1000	TTE
SGRB	2.5	8	-4,4	25-300	TTE
LGRB^b	T_{90}	128	$-T_{90},2T_{90}$	25-300	TTE
SFL^c	60.0	1024	-1000,1000 -3500,3500	10-25	CTIME
TRANSNT	12.5	64	-50,50	25-300	TTE

^{a} Time range is given by taking the trigger time as a reference point.
^{b} T_{90} durations are provided by *Fermi* GBM Burst Catalog.
^{c} SFL time range depends on the CTIME data used.

We combined the data of all triggered detectors to obtain the light curve of the event before applying the Bayesian Block algorithm. After the light curve is represented with Bayesian Blocks, the blocks which are longer than the predefined background time length (BKGTL ; see Table 2) are taken as background blocks, and background level is calculated by taking the maximum of the count rates of these blocks (see Figure 3). The blocks which are shorter than this time limit and higher than the background level around the trigger time are taken as burst blocks, and the duration is calculated as the time interval from the start of the first burst block to the end of the last one. Table 2 shows the predefined background time length, time resolution of the original light curves (TRES), time and energy range of the light curves, and the data types used in the duration calculation for each class.

Figure 3 An example light curve of two consecutive SGR bursts. The first panel shows the combined light curve of the triggered detectors (n2 & n10) with 4 ms time resolution in the 10-100 keV range from -10 seconds to 10 seconds by taking the trigger time as reference. The second and third panel show the applied Bayesian Block Representation on top of the light curve with different time scales around the trigger time. Finally, the fourth panel shows the duration of the SGR burst with dashed lines, and the blocks are numbered: Block 1 is the background block; Block 2, 3 & 4 are the burst blocks; and Block 5 is the block which remains between two consecutive events.

Since the focus of this study is the triggered events, the trigger data types (TTE and CTIME) were used. Thanks to the high time (2 μs) and high energy (128 channels) resolution of TTE data, it is the most appropriate data type for both temporal and spectral analysis, which is why the TTE data is mostly preferred in this study. As solar flares by nature are long lasting and their durations exceed the TTE data time range, trigger CTIME data type is more suitable for them. For long enough bursts (some SFLs and LGRBs), the time range of the analysis can exceed the trigger data time range. The T_{90} information in *Fermi* GBM Burst Catalog[3] and duration information in *Fermi* GBM

---

[3]*Fermi* GBM Burst Catalog: https://heasarc.gsfc.nasa.gov/W3Browse/fermi/fermigbrst.html.

Solar Flares Catalog[4] was applied to determine these long events by checking whether the duration provided by the catalogs for each GRB and SFL trigger exceeds the time range of the analysis specified for those classes in Table 2. If so, continuous data (CTTE and CTIME) was preferred.
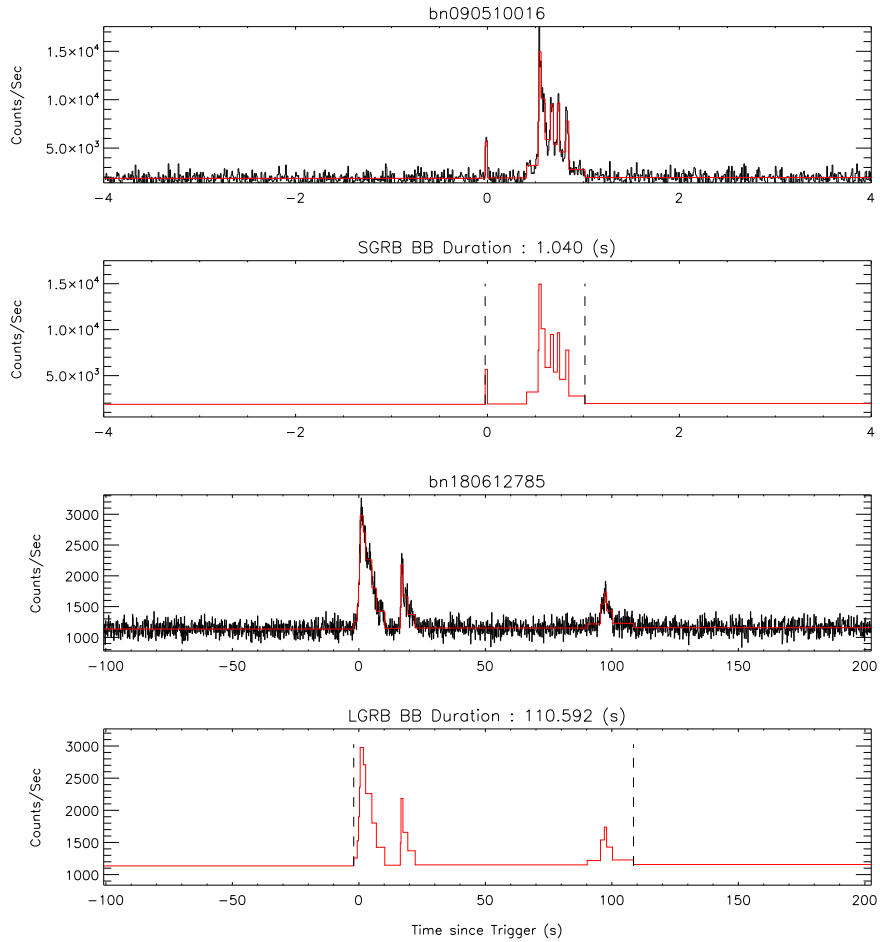
Figure 4 The first panel shows the applied Bayesian Block Representation on top of the combined SGRB light curve of the triggered detectors (n7 & n8) with 8 ms time resolution in the 25-300 keV range from -4 seconds to 4 seconds by taking the trigger time as reference. The second panel shows the Bayesian Block Representation of the light curve and duration of the multi-peaked SGRB with dashed lines. The third panel shows the applied Bayesian Block Representation on top of the combined multi-peaked LGRB light curve of the triggered detectors (n1 & n2) with 128 ms time resolution in the 25-300 keV range from -100 seconds to 200 seconds by taking the trigger time as reference. Finally, the fourth panel shows the Bayesian Block Representation of the light curve and the duration of the LGRB with dashed lines.

The duration calculation of a short burst is more straightforward with Bayesian Block Representation (Lin et al. 2013) compared to a long one as background fluctuates less in a short time period. Therefore, short durations of SGR bursts and TGFs, both of which

---

[4]*Fermi* GBM Solar Flares Catalog: https://heasarc.gsfc.nasa.gov/W3Browse/all/fermigsol.html.

also tend to be single-peaked, can be easily obtained with this technique. In addition, between two successive SGR or TGF events, block lengths can be shorter than the estimated background block length and block count rates between the two are prone to be slightly higher than background level. For those cases, 1σ background error was added to the background level to distinguish two consecutive events. Figure 3 shows an example of how two successive bursts from SGR J1550–5418 on 22 October 2009 presented in Collazzi et al. (2015) separated with addition of 1σ background error to background level.
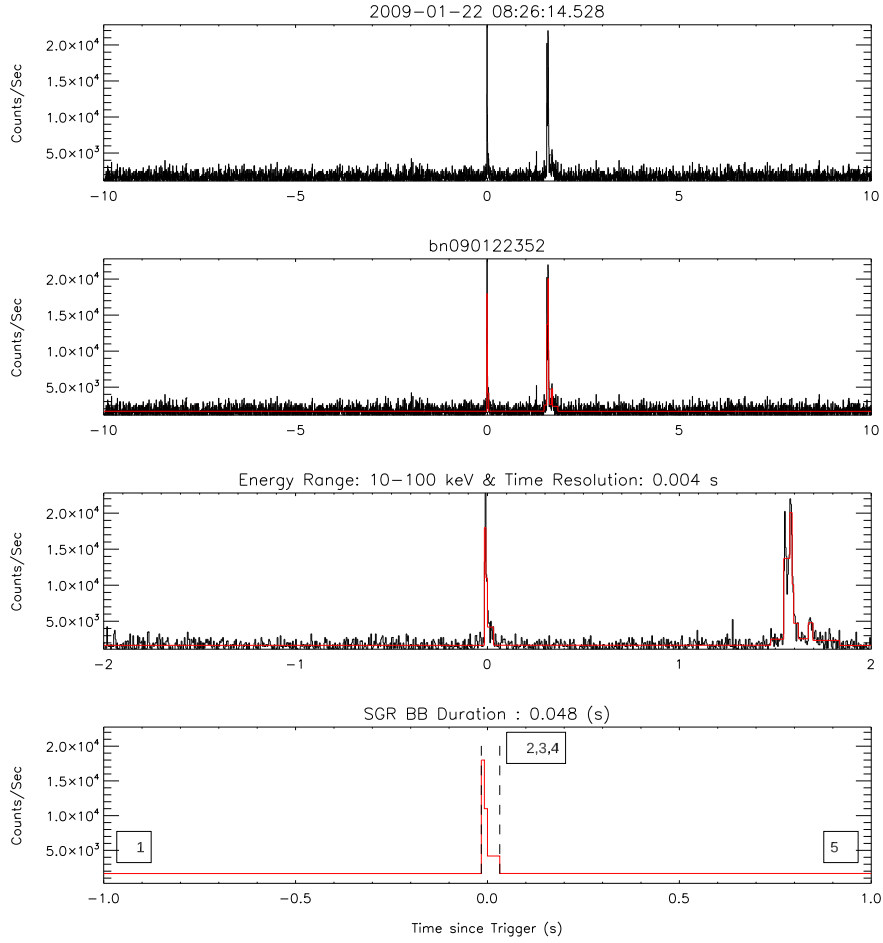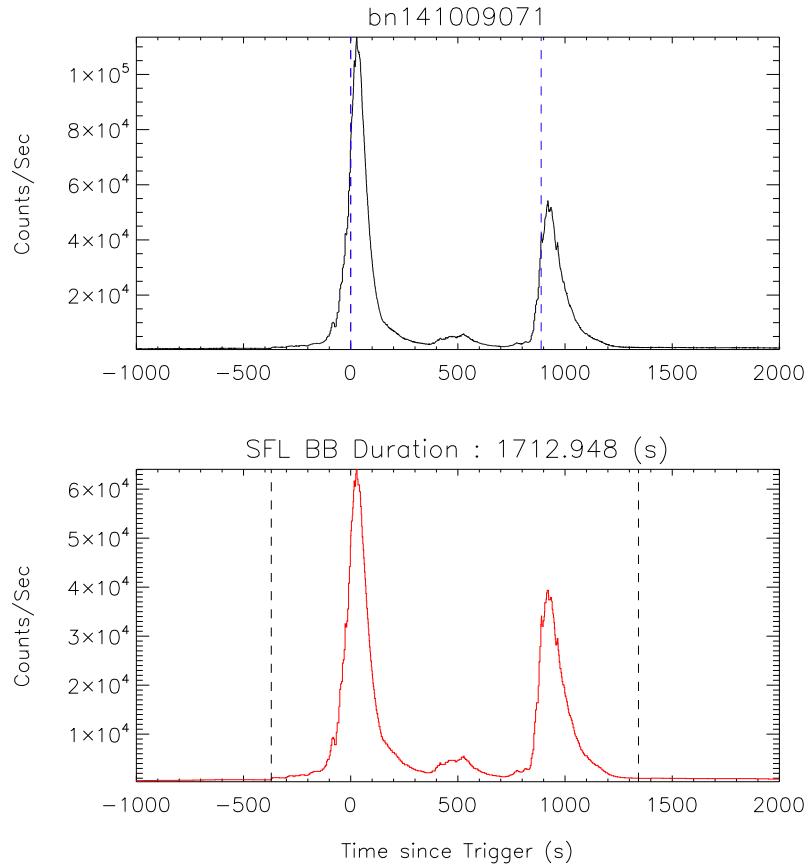

Figure 5 An example light curve of two consecutive SFL triggers. The first panel shows the combined light curve of the triggered detectors (n2 & n5) with 1024 ms time resolution in the 10-25 keV range from -1000 seconds to 2000 seconds by taking the first trigger time as reference. Blue vertical dashed lines indicate the two trigger times. The second panel shows the Bayesian Block Representation of the light curve and the duration of the SFL with dashed lines.

In addition, for TGF triggers, we included triggered BGO detectors in the duration analysis since more than half of them were detected with BGO detectors. Also, unlike Fermi GBM TGF Catalog[5], we used 1 ms time resolution for TGF durations, which are typically up to 1 ms, because durations we obtained with this resolution are sufficient for our classification purpose as other classes do not have such short durations.

---

[5]Fermi GBM TGF Catalog: https://fermi.gsfc.nasa.gov/ssc/data/access/gbm/tgf/.

As stated above, BB duration calculation of long events can be more difficult. For example, GRBs can be multi-peaked events, which means that count rates during the event can come to the background level and rise again. This situation makes the GRB duration calculation complicated, especially for long GRBs. Time interval between the two peaks can be long enough to be included to the background blocks, which yields a shorter duration result than the actual one. In order to avoid these occasions, T_{90} durations were used as estimated background time lengths for LGRBs. Figure 4 exhibits both multi-peaked SGRB and LGRB examples, each with count rates coming to the background level between the peaks during the burst. In addition to GRBs, SFLs can be multi-peaked and trigger the GBM more than once during a prolonged flare. For those cases, triggers were merged and only one duration calculation was performed. Figure 5 is an example of SFL that occurred on 09 October 2014 and triggered the GBM two times.

2.2 Hardness Analysis

Hardness Ratio (HR) which could be used for event classification is simply the ratio of background subtracted counts in two different energy bands: hard and soft. The duration information sufficiently constraints the possible event type list. Together with the spectral hardness, it is possible to assign an event to the class it belongs to with a higher probability. Therefore, we calculated the hardness ratio for each trigger: one at the time of the trigger and another at the peak of the event, as HR can change and evolve during the event.

Before hardness calculation at the time of trigger and peak, the light curve was obtained by combining the TTE data of all triggered detectors with 4 ms time resolution (1 ms for TGFs) in the energy range of 10 - 2000 keV for each triggered event. To obtain the light curve, the time range and data type specified for each class in Table 2 were also used for the hardness analysis. In addition, duration results were included in hardness analysis for background subtraction and determination of peak point. For each event, the time intervals of background blocks in BB duration analysis were used for the hardness analysis, and we took the background level as the average of the count rates in these time intervals. After the background subtracted light curve was obtained, the peak point was determined as the peak bin of the light curve within the duration interval.

In order to obtain the spectral hardnesses of the peak and trigger bins, two more light curves were obtained with the same time bin intervals: the one with the energy range from 10 keV to the energy pivot point (E_{piv}) and the other one with the energy range from

E_{piv} to 2000 keV. The same background subtraction method was applied to the two light curves, and background subtracted soft counts and hard counts were obtained. Then, the spectral hardnesses were calculated as the ratio of hard counts to soft counts at the trigger and peak bins. For hardness ratio error calculations, please see Appendix 1.
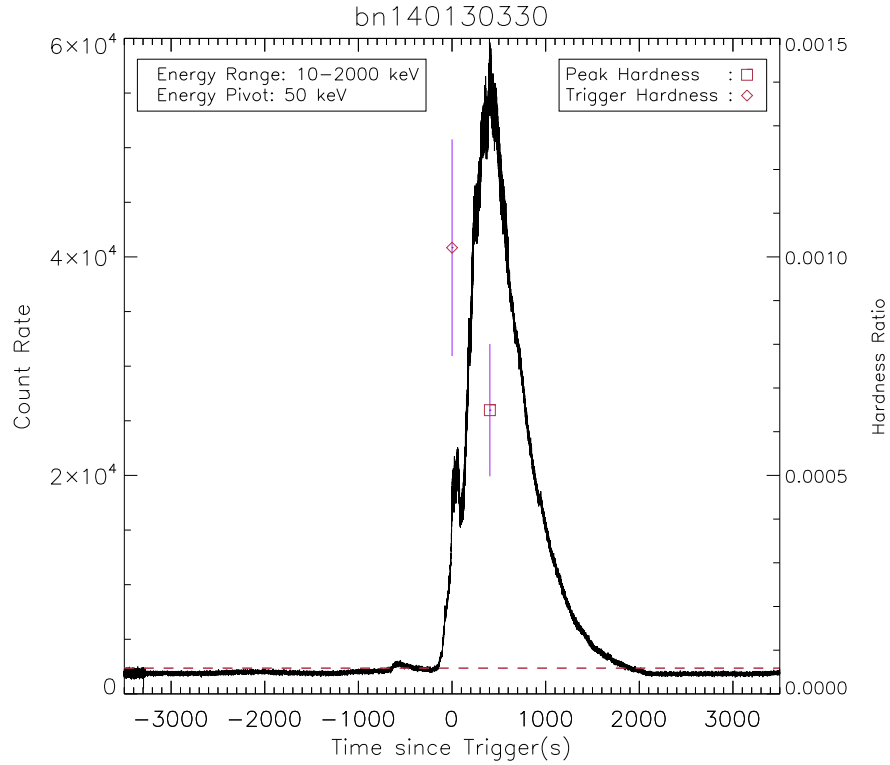
Figure 6 SFL light curve which is obtained with CTIME data of the triggered detectors (n0 & n1) is shown with count rates in the 10-2000 keV range on the left y axis. The horizontal dashed line represents the background level. On the right y axis, hardness ratios of the trigger and the peak with E_{piv} = 50 keV are shown. The vertical solid purple lines represent the hardness errors.

In order to avoid negative counts of background subtracted light curves and to obtain reasonable hardness ratios, we put a constraint criterion in hardness analysis: the hardness ratio must be at least 3 times of its own error (3σ). If this limit can not be exceeded at 4 ms time scale, the hardness ratio was obtained by continuing to apply the same procedure from the beginning with a doubled time scale until the 3σ ratio was obtained.

The CTIME data used for SFLs is quite different from the TTE data because the CTIME data has been already binned into time intervals and packaged with exposure time and count rate in each bin. Therefore, the hardness analysis of SFLs is slightly different. First of all, the count rate in each bin was multiplied with associated exposure time after the background subtraction of the 3 light curves. Thereby, the background subtracted

hard counts and soft counts of the event were obtained. Moreover, the time scales of the trigger and peak bins of a SFL were increased by adding the counts of the next bin instead of doubling the time resolution like in the TTE data case until the 3σ hardness ratio was obtained. Figure 6 shows an example of SFL spectral hardnesses at the time of trigger and peak that are calculated with CTIME data.

Since the main motivation of this study is to find criteria which help the classification of untriggered events in a most efficient way, the selection of E_{piv} is at the heart of this study. Because changing the pivot point means a change in the scales of the soft and hard energy bands, hence a different hardness ratio. Therefore, we searched for the pivot point that allows each class to fall into a different hardness range as much as possible for our classification purpose. Specifically, we aimed to find such an E_{piv} value separately for short event comparison (SGRs vs. SGRBs) and for long event comparison (SFLs vs. LGRBs).
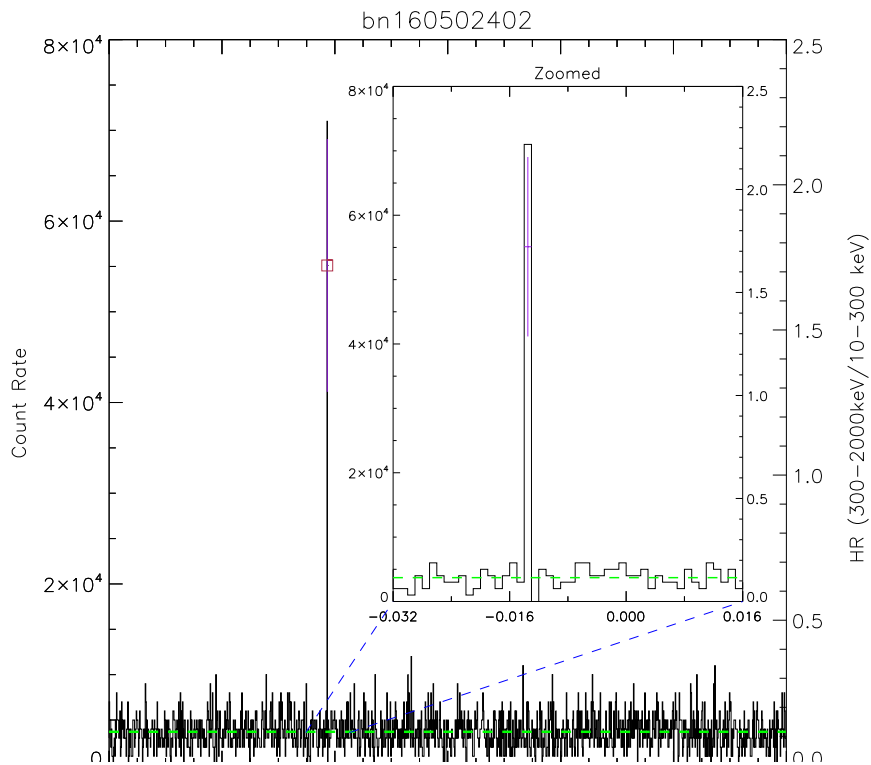
Figure 7 TGF light curve of the triggered detectors (n0 & n3 & n4 & n10) is shown with count rates in the 10-2000 keV range on the left y axis. The horizontal green dashed lines represent the background level. The purple square represents peak hardness with $E_{piv} = 300$ keV. Inside panel zooms around the trigger time and shows the peak hardness value with its error. The event remains on the left side of the trigger time since the trigger time scale is 16 ms.

In the search of E_{piv}, the spectral hardnesses of all triggered events were calculated by using the TTE (CTIME for SFLs) data energy channel edges within 25 - 100 keV range

as pivot points. Then, at each E_{piv}, the number of events within the overlap of the spectral hardness distributions of different classes was calculated separately for short ($\lesssim 2$) and long ($\gtrsim 2$) lasting events. Finally, the pivot points which minimize the number of events from different classes that fall under the same hardness range were identified. In addition to minimization of the overlap, the number of events that could not produce hardness ratio due to either negative or low counts was also taken into account for the E_{piv} selection.
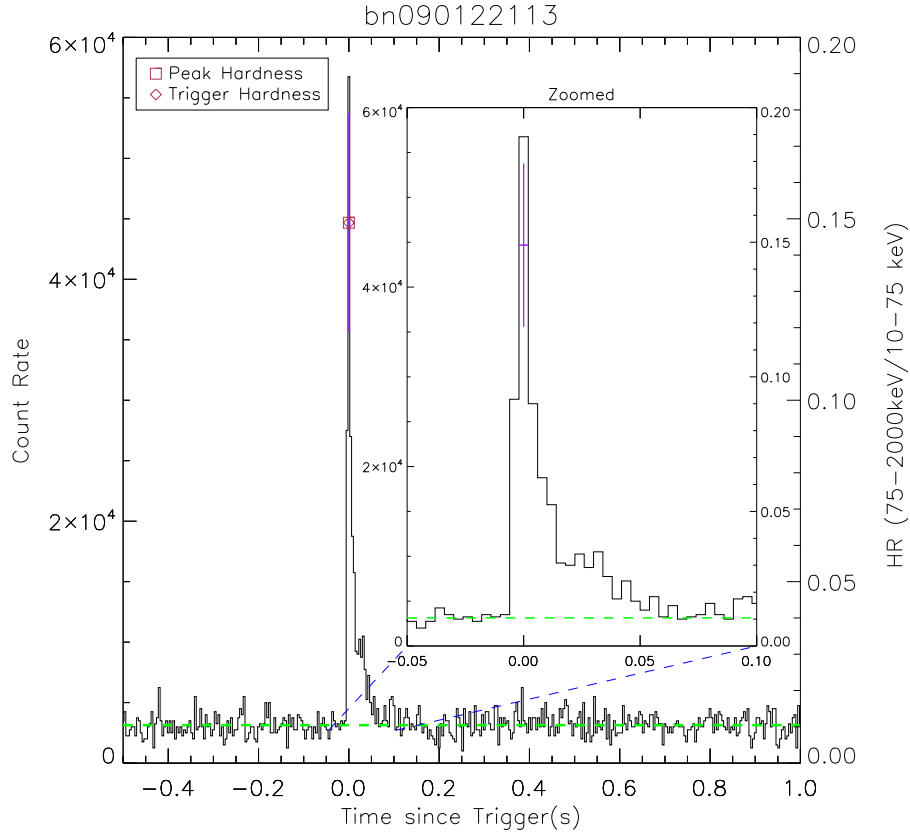
Figure 8 SGR light curve of the triggered detectors (n6 & n7 & n9) is shown with count rates in the 10-2000 keV range on the left y axis. The green horizontal dashed lines represent the background level. Inside panel zooms around the trigger time and shows the peak hardness value with its error. The fact that trigger and peak bins are the same yields only one hardness result.

Most of the TGFs did not produce spectral hardness with any Epiv in the range of 25 - 100 keV due to negative/low counts in the soft energy band after background subtraction. Therefore, we increased E_{piv} to 300 keV, which is also one of the energy channel edges of the TTE data. Nevertheless, we could not still calculate the spectral hardness of half of the TGFs because it is difficult to obtain 3σ hardness value within 1 ms TGF duration. Based on this, 3σ was reduced to 1.5σ and almost all TGFs produced spectral hardness under these criteria. Furthermore, a TGF was included into hardness analysis only if at least one of the NaI(Tl) detectors was triggered. The ones which triggered only the BGO detectors

were eliminated for the goodness of the comparison with the other classes. Finally, we calculated only the peak hardness for TGFs. The duration intervals of TGFs do not involve the trigger time, as TGFs are detected with 16 ms time scale by FSW but our duration and hardness analysis has 1 ms time scale as shown in Figure 7.

The light curves of SGR bursts rise fast and decay exponentially. This leads to the trigger and peak times being close to each other, which increases the probability that the trigger and peak times are in the same bin and hence yield the same hardness ratio. Thus, most of the SGR spectral hardnesses at the trigger and peak have one-to-one correspondence (see Figure 8).

Finally, for TRANSNT hardnesses, we first eliminated the triggers due to sources that either exit Earth occultation or enter outburst periods, which both cases are classified as TRANSNT triggers (see Section 2.4). There remained 20 TRANSNT bursts to be included in duration and spectral hardness analysis. Their durations are 11.96 seconds on average, thereby, TRANSNTs are evaluated as long duration events in the hardness comparison.

2.3 Differentiation of Particle Events

Particle events mostly originate from the charged particles trapped by the Earth's magnetic field. Thereby, the McIlwain L coordinate (geomagnetic latitude; McIlwain 1966) is an important tool for the classification of these geomagnetically trapped particle events. The McIlwain L coordinate (L-shell) represents a particular set of magnetic field lines that cross the Earth's magnetic equator at a certain distance from the center of Earth's magnetic field. In other words, it is the equatorial radius of a magnetic shell in the units of Earth's radius.

The McIlwain L coordinate is used for identification of onboard triggers of particle events (Briggs et al. 2007). Based on this information, we used the *Fermi*/LAT data, which provides the information of spacecraft position averaged over a specified time range with associated L-shell value. Figure 9 presents the closest known position information of the spacecraft at the time of LOCLPAR and GRB triggers. As can be seen from the figure, LOCLPARs mainly occur either around the SAA region or high L-shell values. On the other hand, a GRB is equally probable to trigger *Fermi* at any position or L-shell. Nevertheless, GRBs mostly trigger *Fermi* at low L-shells since the orbit of spacecraft is most of the time at low ones. For checking purposes, we also manually calculated the

L-shell values for all trigger times, using the codes provided by SPEDAS[6] for the space physics community.
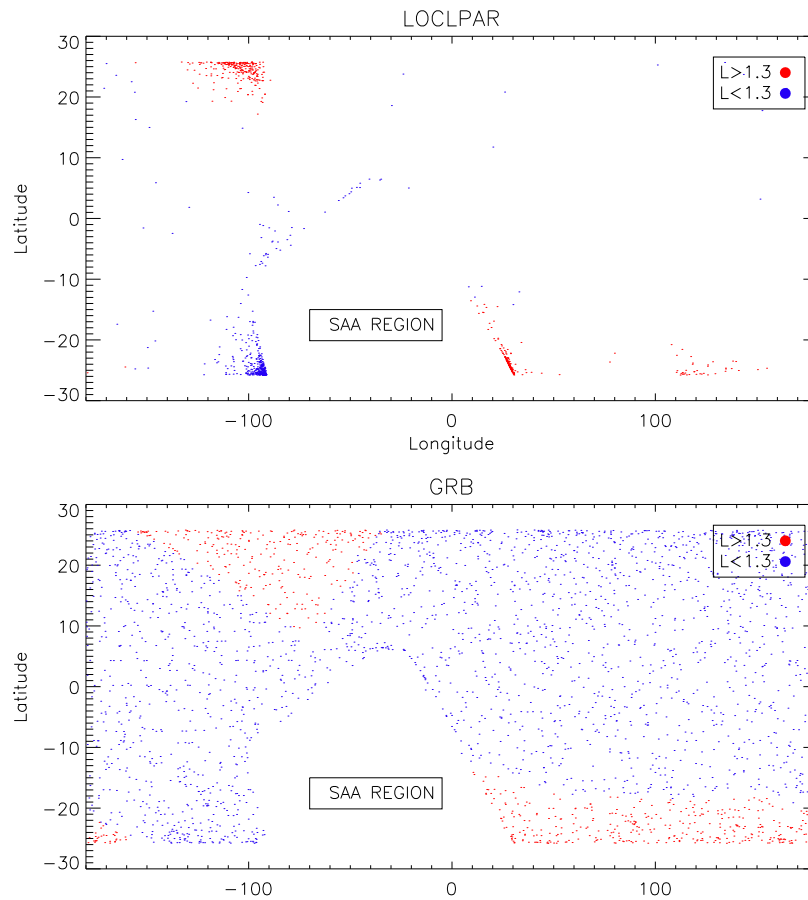
Figure 9 The latitude and longitude of the spacecraft at the times of LOCLPAR (top figure) and GRB (bottom figure) triggers. Blue and red colors represent the low and high L-shell values, respectively. The SAA region is empty (no trigger) since the spacecraft is closed during the SAA passage. L = 1.3 was taken as a dividing value because particle events are observed above this value if they do not occurr in the entrance of SAA or are not caused by cosmic rays.

In addition to the McIlwain L coordinate, max-min ratio is a distinctive method for identifying local particle events, which is also used by FSW for onboard triggers (Briggs et al. 2007). Since local particle events occur most frequently near the spacecraft, they can be seen by all detectors, which means that the expected ratio of maximum and minimum count rates seen by all detectors at the trigger time bin should be around unity. In order to calculate max-min ratio, we used various energy ranges and time scales and searched for unique values so that this method can be easily applied and particle events can be easily distinguished from the others. We found that the max-min ratio of a particle event became closest to unity when we used 50-300 keV energy range and 4096 ms timescale. These values also correspond to values of the trigger algorithm of FSW that detects these

---

[6]SPEDAS: https://spedas.org/blog/.

charged particle events. However, when we applied this time scale and energy range to all triggered events, we found that ratios of all triggers were much closer to 1 than expected due to either energy range or time scale. Therefore, we concluded that there is no unique time resolution and energy range to differentiate particle events from other classes although the trigger algorithm of FSW that detected most of the events in each class could be used as a hint (see below).

There are 120 different trigger algorithms, and each of these has a particular energy range, time scale, and threshold. The timescales start with 16 ms up to 8.192 s as multiples of 16 ms, and the energy ranges are: 25-50 keV; 50-300 keV; >100 keV; and >300 keV. A table of the trigger algorithms can be found in Von Kienlin et al. (2020). TGFs, for example, generally trigger the spacecraft with 16 ms time resolution in the energy range of 300-2000 keV while SGR triggers are mostly in 25-50 keV range with millisecond timescales similar to SFLs (Von Kienlin et al. 2014). However, since these events are seen by only a few detectors, it is expected that the max-min ratio of the count rates of all detectors with the energy ranges and time resolutions in which they are detected by FSW is much higher than one. On the other hand, the max-min ratio of local particle events observed by all detectors in the 50-300 keV energy range and 4096 ms time resolution are expected to be close to one. Therefore, we applied the triggered energy ranges and time scales to calculate the max-min ratios.

2.4 Subclasses of Transient Triggers

Some of the TRANSNT triggers are due to known active X-ray sources. The active periods of these (pulsating) sources are well known and can be easily matched to the trigger times. Therefore, we developed an algorithm to identify the sources of TRANSNT events. Since our project provides for creating a database for identifying the sources of untriggered events, triggers caused by such known sources were identified and excluded from our analyses.

In 2015 and 2017, the outbursts of V404 CYG and Swift J0243.6+6124 triggered the *Fermi* numerous times (Von Kienlin et al. 2020). Based on this information, the triggers due to these outbursts were decided by using the position information of these sources and the spacecraft. Since the position and orientation of *Fermi* at the trigger time is provided with position history files, the angles between the detectors' zeniths and the source can be obtained. If the triggered detectors see the source with the smallest angles compared to the untriggered ones, this means that the trigger most likely originates from that source.

Figure 10 presents the light curve of a triggered TRANSNT event, bn171102658, which is most probably triggered by a pulsating source, Swift J0243.6+6124.

Figure 10 12 detectors light curves of a TRANSNT event, bn171102658, in the 25-50keV energy range with 64 ms time resolution. Red lines represent the Bayesian Block Representation. This is an example light curve from the outburst of Swift J0243.6+6124.

The sources coming out of Earth occultation create a sudden increase in the detectors' count rates, thereby they are able to trigger the *Fermi* and these triggers are classified as TRANSNT in the FERMIGTRIG. The position information of the known sources observed by *Fermi* can be found at the GBM team web page[7].

Using the right ascension and declination of these sources and *Fermi*'s position, the rise and set times of these sources with respect to the spacecraft can be determined. The rise and set times refer to the times when the source exits and enters the Earth occultation, respectively. If the rise time of one of these sources are just before the trigger time of a TRANSNT event, it is probable that trigger is caused by that source exiting the Earth

---

[7]The GBM team web page: https://gammaray.msfc.nasa.gov/.

occultation. In addition to that, the triggered detectors must see this source at appropriate angles to confirm the source. Figure 11 shows an occultation light curve example from a trigger, bn180407555, which most probably occurred due to IGRJ 18245-2452.
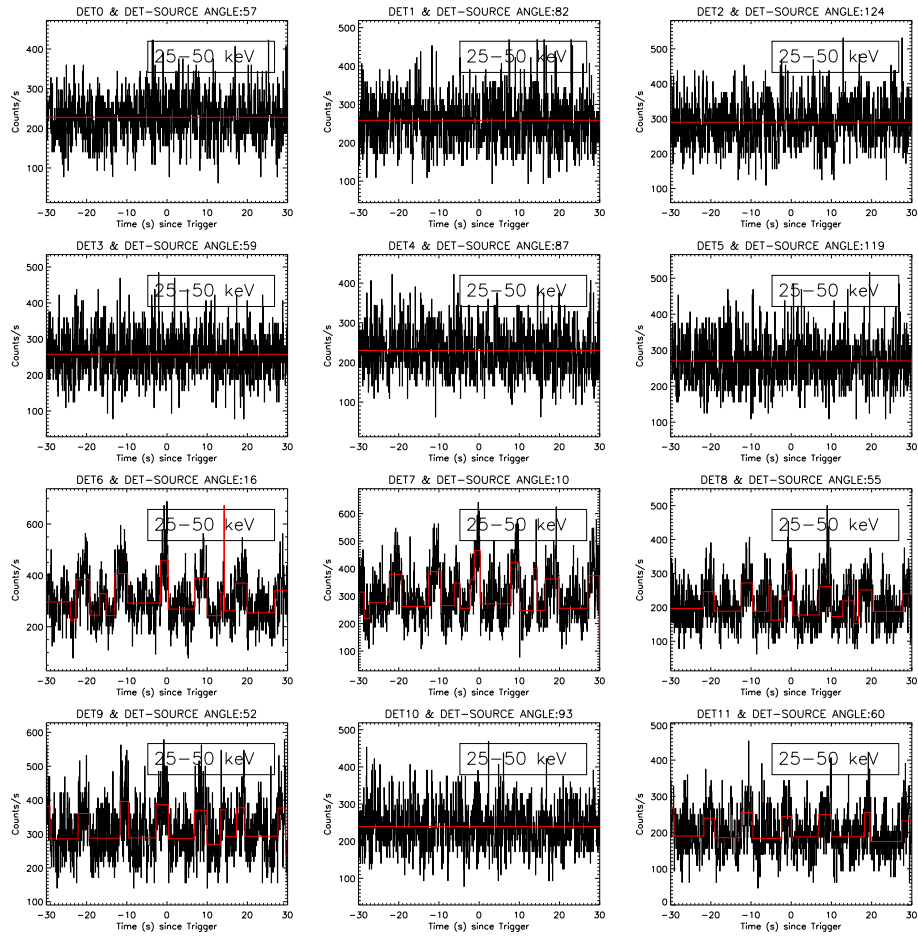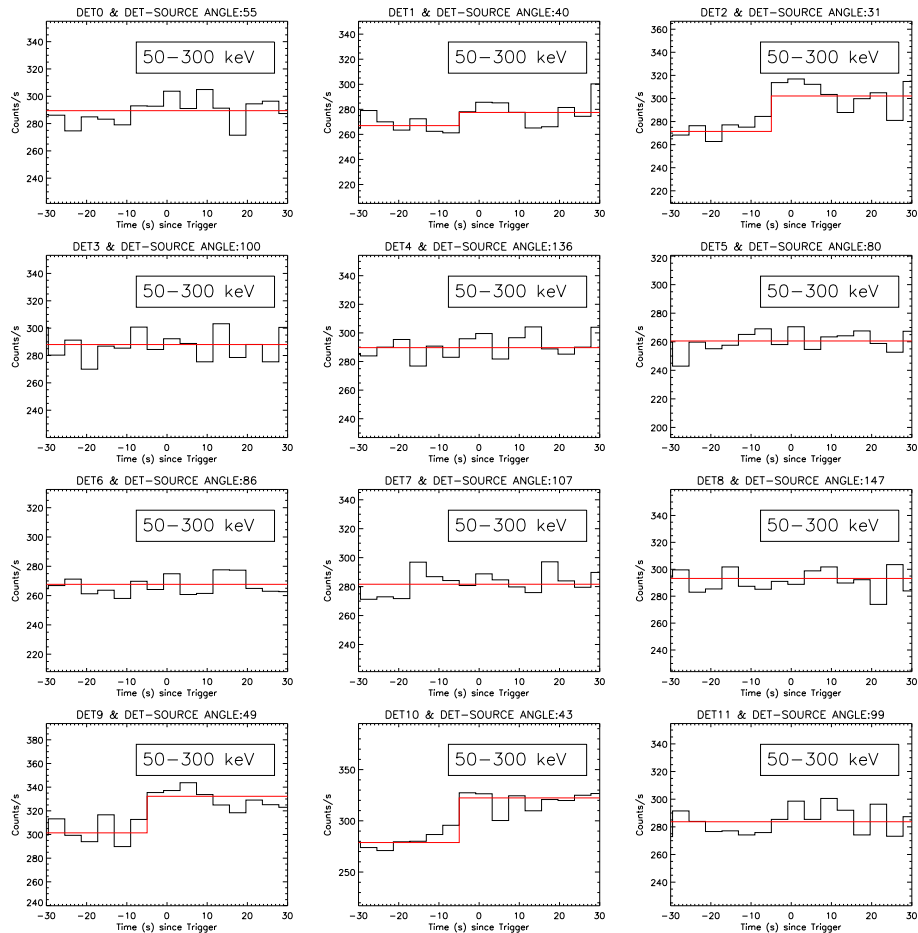

Figure 11 12 detectors light curves of a TRANSNT event, bn18040755, in the 50-300keV energy range with 4-s time resolution. Red lines represent the Bayesian Block Representation. The detectors that observe IGRJ 18245-2452 with the smallest angles show an increase in the count rates and their BB representations seem like a step function.

3 RESULTS & DISCUSSION

We performed the duration and hardness ratio analysis using the data that includes all GBM triggers up to December 31, 2020. For all triggered events, we also performed the max-min ratio and the McIlwain L coordinate methods, which are the methods used for classification of particle events in onboard triggered events. We explain the results of our study in detail in this section.

20

3.1 Duration Results

GRBs: We calculated the BB durations of 2494 triggered GRBs, of which 2011 are longer and 483 are shorter than 2 seconds based on our BB duration results. Figure 12 shows the BB duration distribution of GRBs. The distribution is best described by a lognormal function with a mean duration of 14.018 ± 0.496 s. Figure 12 also shows two more lognormal fits for short and long GRBs separately. SGRBs and LGRBs have a mean duration of 0.586 ± 0.075 s and 18.522 ± 0.622 s, respectively. As can be seen from the figure, their overlapping region is centered at ~ 2 seconds, which is consisted with the T_{90} distributions reported in other studies (Kouveliotou et al. 1993 ; Lien et al. 2016). Also, Figure 13 confirms this consistency with overall duration distribution of our GRB BB results and the T_{90} durations of the same events from *Fermi* GBM Burst Catalog.
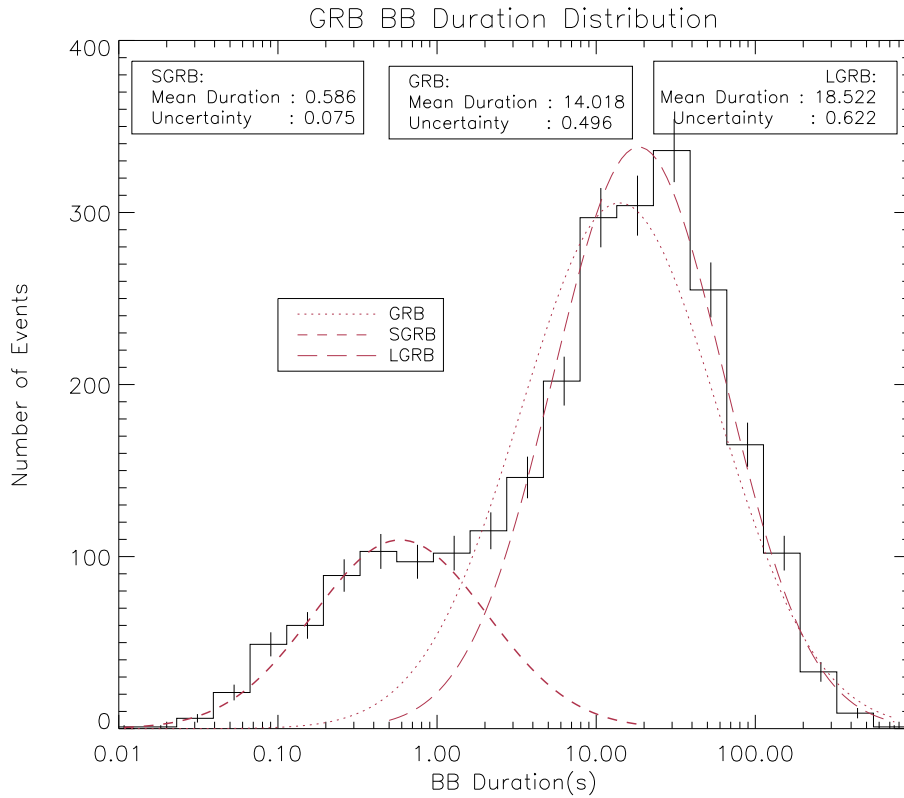
Figure 12 BB duration distribution of GRBs in the 25-300 keV range. Long-dashed line indicates LGRB lognormal fit whereas short-dashed line indicates SGRB lognormal fit. Their intersection is around 2 seconds. Also, the dotted line represents the overall GRB duration distribution.

SGRs: We calculated the BB durations of 317 out of 318 SGR bursts, which is a much smaller sample compared to GRBs. Their BB durations are up to ~ 1 second, and the lognormal fit of the duration distribution peaks at 0.134 ± 0.024 s. Figure 14 presents the distribution of SGR durations and the lognormal fit for this distribution.
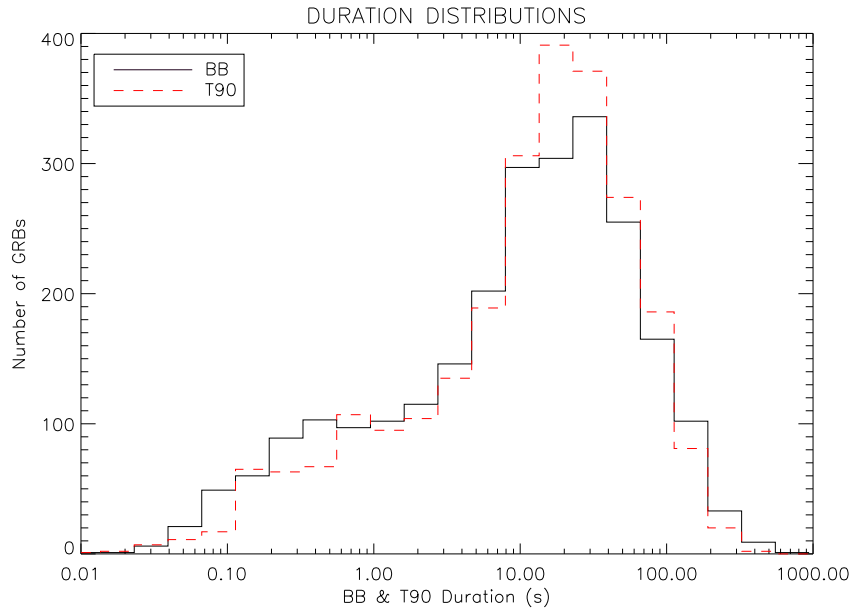
Figure 13 BB duration distribution of GRBs in the 25-300 keV range is represented with black solid line. T_{90} duration distribution of the same events is represented with red dashed lines.
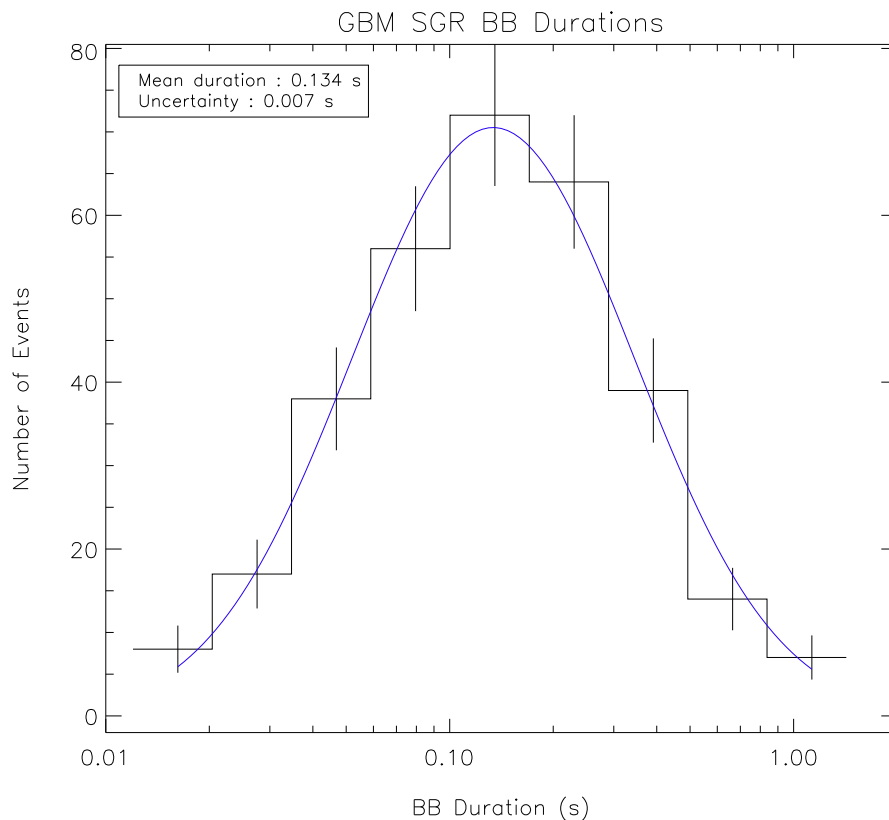
Figure 14 BB duration distribution of SGRs in 10-100 keV range. The blue solid line indicates the lognormal fit of the distribution.

TGFs: We calculated the BB durations of 1026 out of 1092 TGFs and found that 775 out of 1026 TGFs have 1 ms duration and 175 of them have 2 ms duration whereas the remaining 76 last up to a few ms due to their prolonged tails.

SFLs: There exist 1189 SFL triggers. Their BB durations have a wide range from a few tens of seconds to a few thousands of seconds, and their mean is 983.95 seconds. Figure 15 shows the BB duration distributions of both TGFs and SFLs.

TRANSNTs: There are 430 TRANSNT triggers. We identified that 363 of them are due to outbursts of known sources and 47 of them are due to Earth occultations of known sources. There remained 20 TRANSNT bursts, which decrease in number after the outbursts and occultations are cleared and make it difficult to obtain a distribution. Their durations are 10.96 s on average.
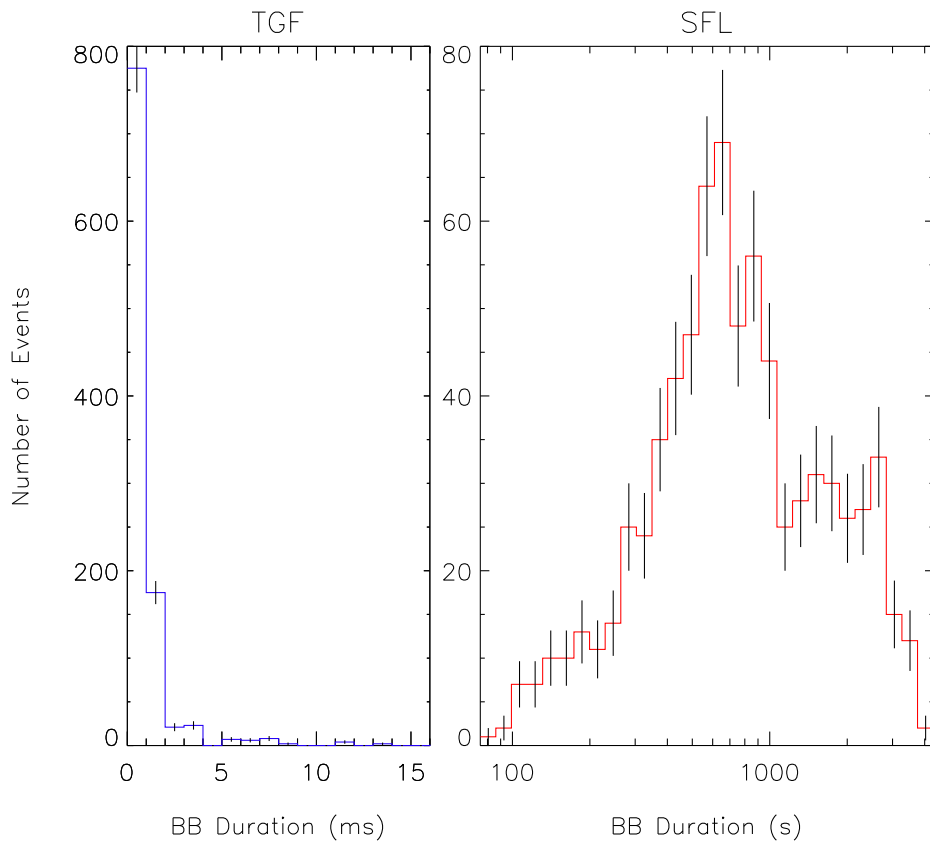
Figure 15 [*Left*] BB duration distribution of TGFs. [*Right*] BB duration distribution of SFLs.

3.2 Hardness Results

Hardness results provide an additional dimensionality for classification after the duration results. Therefore, we calculated the hardness ratio for all event types separately, using the set of E_{piv} values described earlier.

23
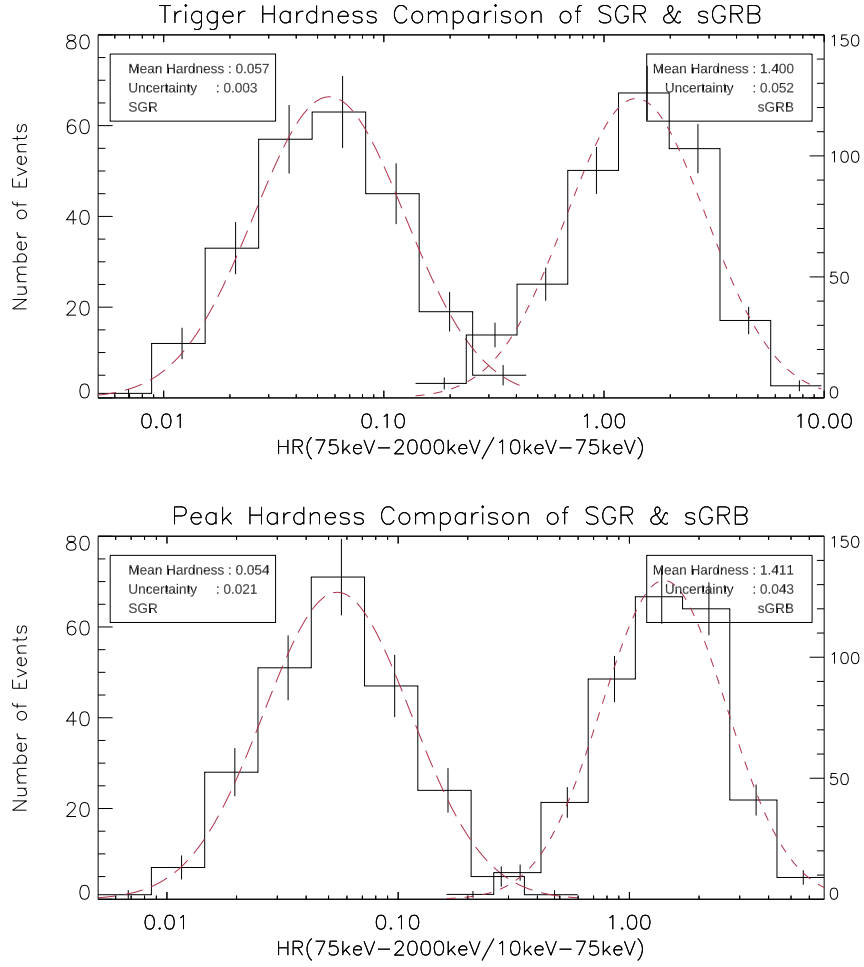
Figure 16 [*Top*] The distributions of hardnesses of SGRs and SGRBs at the trigger time bin. The left distribution belongs to SGRs with the long-dashed line representing the lognormal fit of the distribution. The right distribution belongs to SGRBs with a short-dashed line representing lognormal fit of the distribution. [*Bottom*] The distributions of hardnesses of SGRs and SGRBs at the peak time bin. The left distribution belongs to SGRs with a lognormal fit. The right distribution belongs to SGRBs, also with a lognormal fit.

For hardness ratio comparison of **short events**, 75 keV was selected as E_{piv}. SGRBs are dominant in the energy range of 25-300 keV while SGRs are most powerful in the 10-100 keV range. Therefore, we performed the BB analysis in these energy ranges. Also, this situation naturally means that SGRBs are spectrally harder than SGRs. Hardest SGRs, however, show an overlap with softest SGRBs, which is minimized at 75 keV as E_{piv}. The mean hardness of the SGRB distribution is more than two orders of magnitude larger than that of the SGR distribution both at the trigger and the peak time. SGRs have hardnesses in the range of 0.005 - 0.5 and a mean of 0.057 ± 0.003 at the trigger time and 0.054 ± 0.021 at the peak, while the hardness range of SGRBs is 0.1 - 10.0 and their mean is 1.4 ± 0.052 at the trigger and 1.411 ± 0.043 at the peak. Hence, these events overlap in between 0.1 and 0.5 hardness range centered ∼ 0.3. Figure 16 shows the

hardness distributions of each of these event types at the time of the trigger and the peak, respectively. Additionally, Figure 17 (top panel) shows the HR distributions with $E_{piv} = 75$ keV for short events including TGFs.
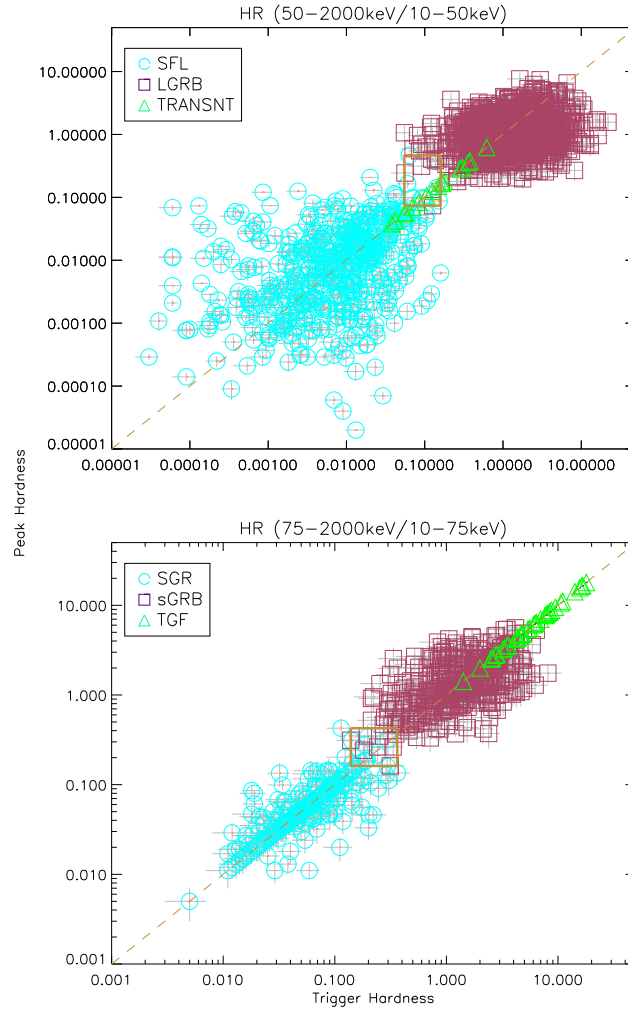
Figure 17 [*Top*] Trigger Hardness vs Peak Hardness Distribution of long events (SFL, LGRB & TRANSNT) at $E_{piv} = 50$ keV. The gold rectangle shows the overlapping area of both trigger and peak hardnesses of SFLs and LGRBs. [*Bottom*] Trigger Hardness vs Peak Hardness Distribution of short events (SGRB, SGR, & TGF) at $E_{piv} = 75$ keV. The gold rectangle shows the overlapping area of both trigger and peak hardnesses of SGRs and SGRBs.

588 TGFs out of 1092 triggered at least one of the NaI(Tl) detectors. However, only 41 triggers out of 588 produced spectral hardness with 75 keV pivot as can be seen from Figure 17. Therefore, we increased E_{piv} to 300 keV for TGFs and almost all TGFs provided reliable HR with this E_{piv} as can be observed in Figure 18. Figure 18 also shows the hardness distribution of TGFs with a lognormal fit. The mean hardness of TGFs is close to unity, similar to the finding of Roberts et al. (2018).
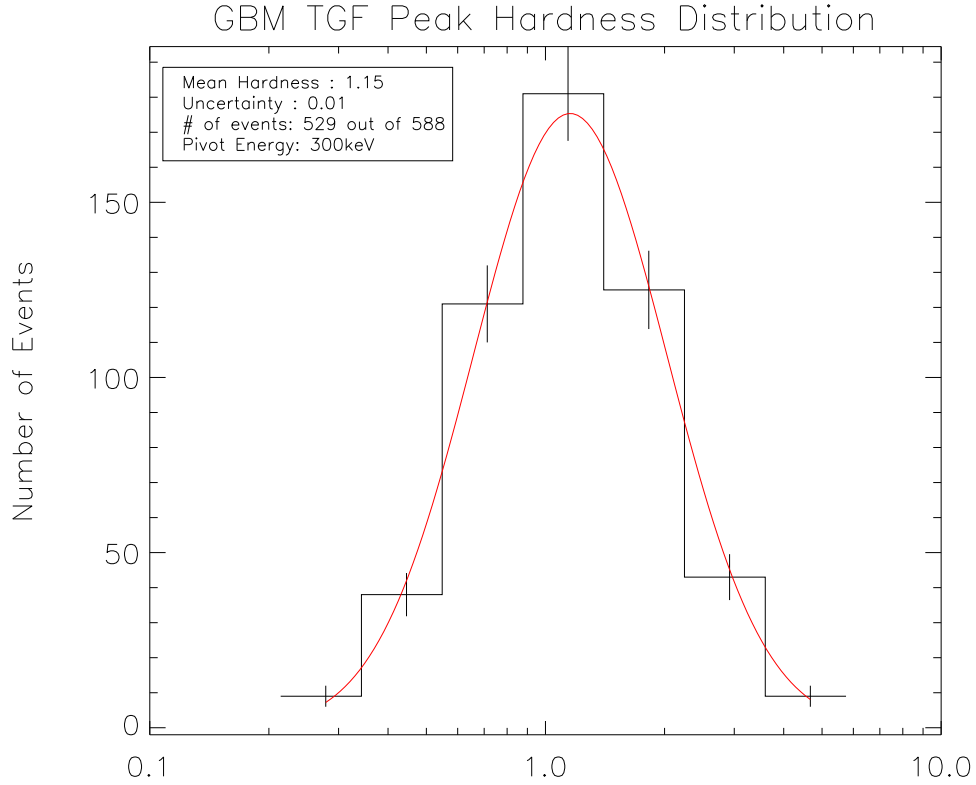
Figure 18 The hardness distribution of TGFs. The red solid line represents the lognormal fit. The mean hardness is 1.15 with an uncertainty of 0.01.

On the other hand, 50 keV pivot was selected for hardness calculation of the **long events** such as LGRBs and SFLs. Figure 19 shows the hardness distributions of SFLs and LGRBs at the time of trigger and the peak together with their lognormal fits, respectively. Almost all GRB events triggered the *Fermi*/GBM in the 50-300 keV range whereas SFL mostly triggered it in the energy range of 25-50 keV. So, it is naturally expected that SFLs are softer than GRBs. However, the overlap of the hardest part of the SFL distribution and the softest part of the LGRB distribution is inevitable at any E_{piv}. The minimum overlap has been obtained at 50 keV by also taking into account that SFLs have been studied with CTIME data. As mentioned before, CTIME data has 8 energy intervals, which is low energy resolution compared to TTE data with 128 energy channels. The mean hardness of the LGRB distribution is more than two orders of magnitude larger than that of the SFL distribution both at the trigger and the peak time. SFLs have a wide hardness range of 0.00005 - 0.5 and a mean of 0.0080 ± 0.0006 at the trigger time and 0.0070 ± 0.0010 at the peak while hardness range of LGRBs is 0.1 - 10.0 and their mean is 1.298 ± 0.026 at the trigger and 1.088 ± 0.015 at the peak. Hence, these events overlap in between 0.1 and 0.5 hardness range centered ∼ 0.3.

Since we have only 20 TRANSNT events, we could not create a distribution. Their hardnesses lie in between the SFLs and LGRBs as shown in Figure 17. They show an overlap with hard SFLs and soft LGRBs, and their average hardness is around 0.2.

Finally, the duration distribution of GRBs points out two sub-classes as short ($\lesssim 2$) and long ($\gtrsim 2$) GRBs as discussed in the duration results. The hardness results reinforce this argument by providing an additional characteristic as 'short-hard' and 'long-soft' GRBs as can be seen from Figure 20.
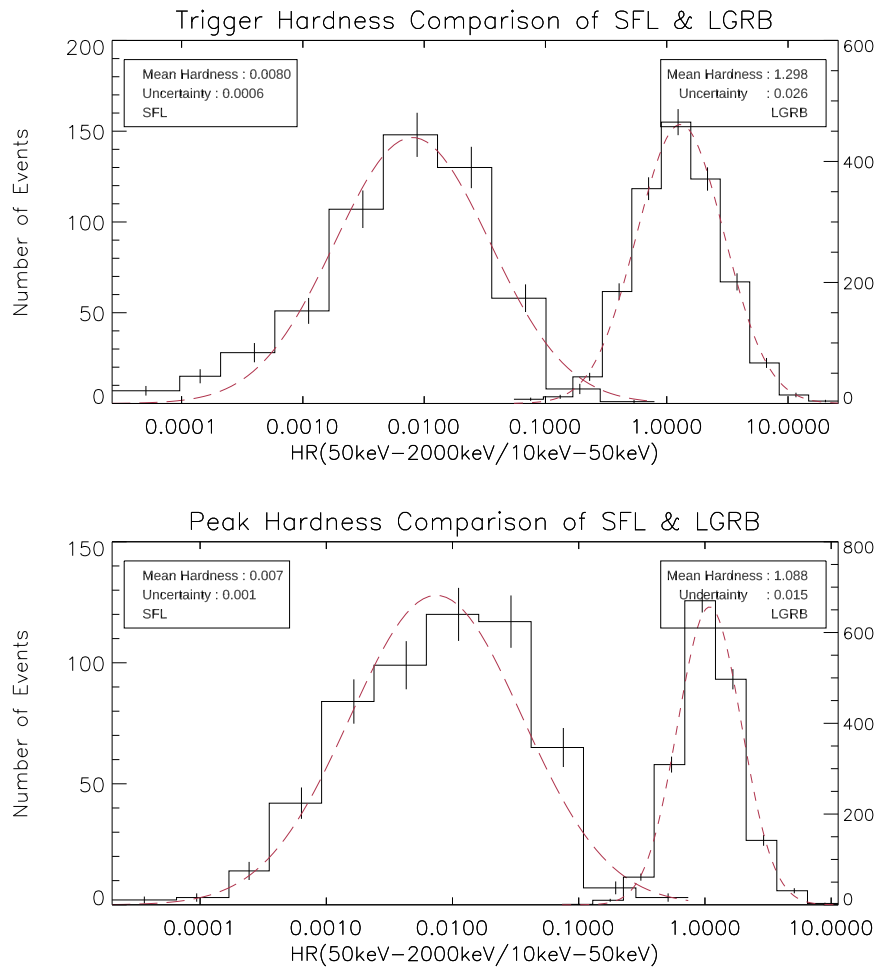
Figure 19 [*Top*] The distributions of hardnesses of LGRBs and SFLs at the trigger time bin. The left distribution belongs to SFLs with the long-dashed line representing the lognormal fit to the distribution. The right distribution belongs to LGRBs with the short-dashed line representing lognormal fit of the distribution. [*Bottom*] The distributions of hardnesses of SFLs and LGRBs at the peak time bin. The left distribution belongs to SFLs with a lognormal fit. The right distribution belongs to LGRBs, also with a lognormal fit.
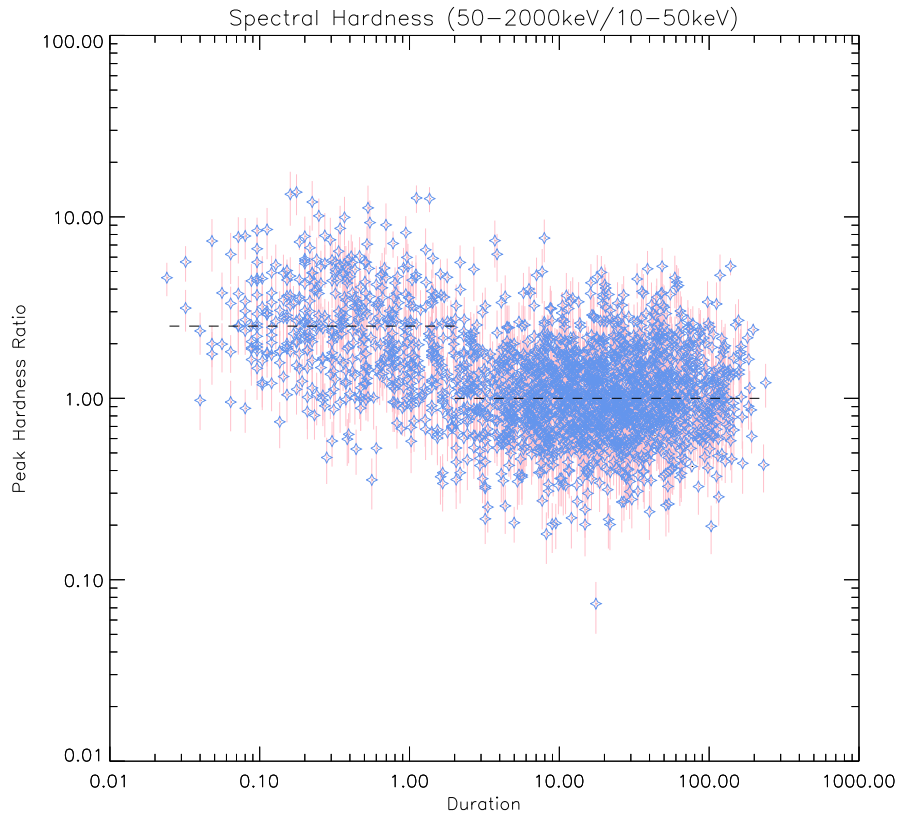
Figure 20 The Duration-Hardness diagram for triggered GRBs. The horizontal dashed lines represent the mean hardnesses of short (<2) and long (>2) GRBs, respectively.

3.3 L-Coordinate Results

The McIlwain L coordinate results showed that the particle events which triggered *Fermi*/GBM at low shell values mostly occurred just before the entrance of *Fermi* to the SAA region. On the other hand, the remaining ones occurred at high L-shell coordinates including the exit region of the SAA. Figure 21 shows the comparison of distributions vs. the McIlwain L coordinates of GRBs and LOCLPARs. Although GRBs are equally likely to trigger the *Fermi*/GBM at any coordinate, they occurred at low shell values due to spacecraft orbit. LOCLPARs are, however, most likely to occur around the SAA region or at high L-coordinates. Moreover, the distributions of other classes such as SFLs, TGFs, and SGRs are similar to GRBs, hence the GRB example here represents the distribution of each event type against particle events.

In addition to LOCLPARs, 67 out of 82 DISTPAR triggers occurred at high (> 1.3) McIlwain L coordinates while half of the remaining events triggered the *Fermi*/GBM around the SAA entrance.
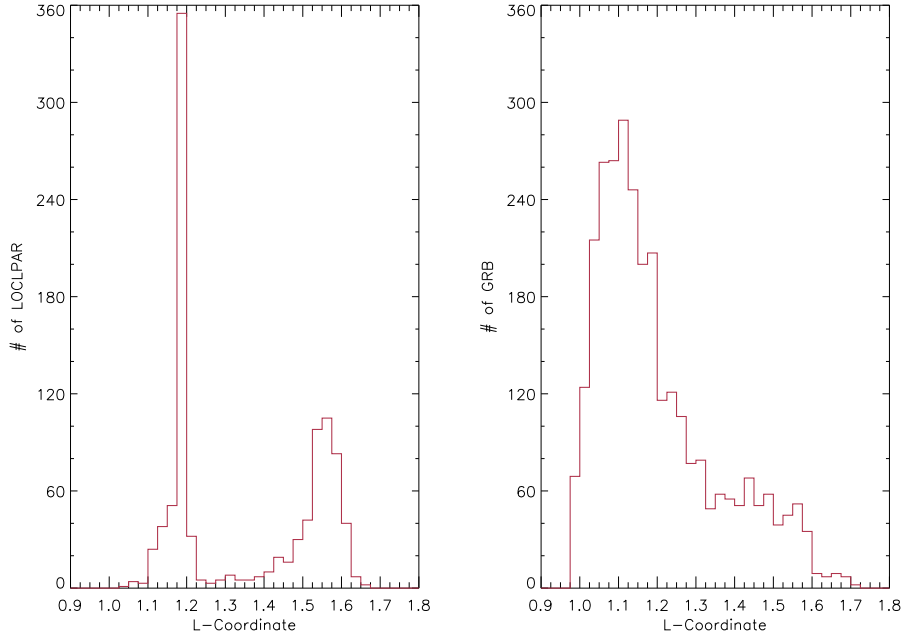
Figure 21 [*Left*] The distribution vs. L-shell coordinates of LOCLPARs from the entire mission that triggered in orbit. [*Right*] The distribution vs. L-shell coordinates of GRBs from the entire mission that triggered in orbit.

3.4 Max-Min Ratio Results

To obtain the max-min ratio values, we plotted the event light curves using various energy ranges and time scales, and we found that a particle event's light curves in the 12 NaI(Tl) detectors of the GBM are quite similar to each other in the time scale of 4096 ms and the energy range of 50-300 keV, as also reported by Jenke et al. (2016). Hence, the count rates at the trigger time bins are close to each other, which yields the max-min ratios of right above 1. However, it is not possible to differentiate these particle events with a single time resolution, since the max-min ratio of a short lasting event such as SGR or TGF also approaches 1 as the time scale increases. Thus, we took advantage of trigger algorithms, each with a specific energy range and time scale.

Particle events were mostly detected by FSW in the 50-300 keV energy range and 4096 ms time scale, similar to our findings. On the other hand, events with shorter duration triggered the detectors with short time scales at various energy ranges. Therefore, using the energy ranges and time scales at which events are detected results in more efficient comparison of the max-min ratio of the classes. As a result, the max-min ratio of events such as TGFs, SGRs and SFLs are frequently well above two, while the ratios of particle events are below 2.

29

The energy range of 50-300 keV is also the range in which GRBs are observed besides charged particle events. These two event types, however, differ in that GRBs are seen by only a few detectors unlike local particle events. Nevertheless, the distribution of max-min ratios of GRBs, shows an overlap with that of the local particle events. Even if these two event types can be distinguished by looking at the light curves in the 12 detectors, it does not seem possible to easily detect this difference by calculating the max-min ratio as clearly seen in Figure 22. In addition, max-min ratios of GRBs detected with high time scales by FSW show more overlap with the ones of particle events than those detected with low time scales. We will need additional parameters such as the number of triggered detectors or spectral parameters in order to distinguish these two event classes at a sufficient confidence level.
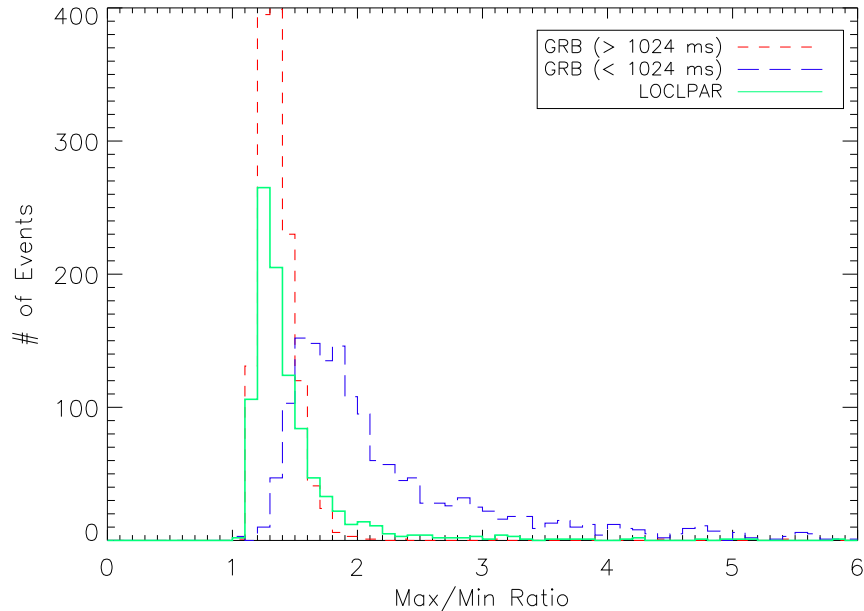
Figure 22 The distribution of max-min ratios of LOCLPARs represented with a green solid line and the distribution of max-min ratios of GRBs detected with lower and higher than time scale of 1024 ms represented with blue long-dashed and red short-dashed lines, respectively.

Finally, DISTPARs, which occur on the Earth horizon, are seen by only a few detectors unlike local particle events, so max-min ratio does not help to differentiate these events. In addition to magnetic L coordinate, the second method for differentiation of distant particles can be to check whether they occur on the Earth limb or not. This second method, however, needs further investigation.

4 CONCLUSION & FUTURE PROSPECTS

With the aim of defining well-constraint parameter distributions for the classification of events found in untriggered-event searches, we studied in detail the classified events in the *Fermi*/GBM Trigger Catalog up to December 2020. The gamma-ray transient events that are likely to be found with untriggered-event searches in the *Fermi*/GBM data are GRBs, SGRs, TGFs, SFLs, TRANSNTs, and charged particle events.

First of all, we performed duration and hardness analysis, respectively. Based on the duration results, we divided all event classes into two categories as short and long events. Short events consist of SGRBs, SGRs and TGFs, whereas long ones include LGRBs, SFLs, and TRANSNTs. For each category, we took advantage of spectral hardness results and determined Epiv that produces the least overlap in the hardness distributions of the event classes for an efficient classification. We obtained the E_{piv} of 50 keV for long and 75 keV for short events, respectively.

BB durations of GRBs show that these events can last from a few milliseconds to hundreds of seconds, and their duration distribution indicates two subclasses of GRBs as short and long GRB. In addition, the lognormal fit of the BB duration distribution reveals that this division is at ~ 2 seconds. Moreover, SGRBs tend to be spectrally harder than LGRBs. The lognormal fits of their spectral hardness distributions with both $E_{piv} = 50$ keV and 75 keV show that the peak of the hardness ratios of SGRBs is more than two times higher than the peak of LGRB hardness ratios.

TGFs are the shortest and spectrally hardest events among the gamma-ray transient events in this study. Their durations are typically less than a millisecond, or, very rarely up to a few milliseconds due to their prolonged tails. We performed their duration analysis in 1 ms time scale and calculated the durations of the submillisecond events as 1 ms, since none of the classes except TGFs have 1 ms duration. In addition, TGFs did not produce spectral hardness at $E_{piv} = 75$ keV due to the negative/low counts in the soft energy band after background subtraction in their short time periods. So, we increased E_{piv} to 300 keV, calculated the spectral hardness over the entire duration and found their mean hardness as close to unity.

In addition, we observed that BB duration distribution of SGRs and SGRBs have a similar duration range from a few milliseconds to a few seconds, with a mean of 0.134 s and 0.586 s, respectively. Therefore, we compared their spectral hardnesses at $E_{piv} = 75$

keV and found that SGRs have hardnesses in the range of 0.005 - 0.5 and the hardness range of SGRBs is 0.1 - 10.0. The mean hardness of the SGRB distribution is more than two orders of magnitude larger than that of the SGR distribution.

Similarly, we compared the spectral hardnesses of long events such as SFLs and LGRBs at E_{piv} = 50 keV and found that the SFLs have a wide hardness range of 0.00005 - 0.5 and the hardness range of LGRBs is 0.1 - 10.0. The mean hardness of the LGRB distribution is more than two orders of magnitude larger than that of the SFL distribution. Moreover, since TRANSNT bursts are 10.96 s on average, we compared their spectral hardnesses with long events. Their hardness ratios have a mean of 0.2 and lie in between SFLs and LGRBs.

For the identification of SFLs, catalogs such as *Fermi*/GBM Solar Flare Catalog can be used prior to time and hardness analysis, since these events are well known and well studied. This catalog, which is a dynamic catalog and updated as new flares are identified, provides information on the time interval of the flare and that which detectors observe the flare. Thus, it can be checked whether an event found in untriggered-event searches falls into the time interval of any SFL. If so, it can be further checked whether the triggered detectors match with the detectors announced by the catalog. However, the triggered detectors may not match since the sun is a close source and can affect many detectors unlike a distant source. Then, for those cases, the duration and hardness analysis will be helpful to identify a SFL.

Secondly, we differentiated particle events with the help of the McIlwain L coordinate of the spacecraft and maximum to minimum ratio of the count rates of the 12 NaI(Tl) detectors of the GBM at the time of trigger. Since charged particle events have typically magnetospheric origin or occur rarely due to cosmic-ray showers, the McIlwain L coordinate of the Fermi is the most important tool for classification of both local and distant particle events. These events occur either around the SAA region or the high (>1.3) L shell values. Moreover, we tested a second classification method, the max-min count ratio for local particle events, since their light curves hence the count rates in the whole NaI(Tl) detectors of the GBM are quite similar to each other in the energy range of 50-300 keV. However, the efficiency of this method depends on the number of modes in which the untriggered-event searches are performed, each with a specific energy range and time resolution. Since each mode targets a particular event class or classes, the mode in which an event is found but not in the others gives a clue about the class of that event hence the expected max-min ratio. On the other hand, for a distant particle event, an alternative secondary differentiation mechanism (instead of min-max ratios) can be to check whether the trigger occurs at the Earth horizon.
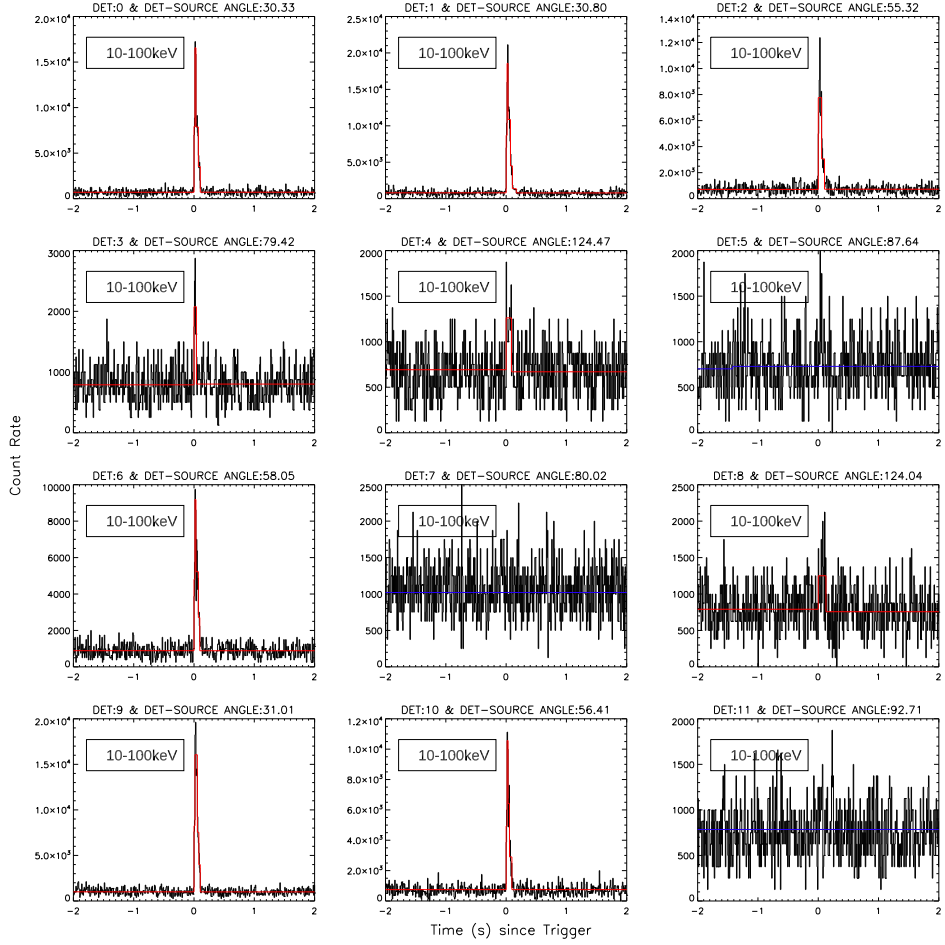
Figure 23 12 detectors light curves of the example SGR burst found in the untriggered event search in the 10-100 keV energy range with 8 ms time resolution. Red lines represent the Bayesian Block Representation of the "triggered" detectors. The blue lines represent the "untriggered" ones. The detectors (n1, n0 & n9) that observe SGR 1935+2154 with the 3 smallest angles ($\sim 30°$) are the brightest ones.

Finally, we developed an algorithm to eliminate the pulsation and Earth occultation triggers of the known sources from the transient bursts with the help of the GBM accreting pulsar histories and the GBM occultation flux histories data provided by the GBM team. The pulsar data includes the list of known pulsars observed with Fermi, their positions and periods, and outburst detection times. This data can provide us a way to distinguish a big portion of events due to pulsations found in untriggered-event searches, by checking whether the trigger time falls under outburst period of any of the sources. If so, we can further check whether the triggered detectors see the source with smallest angles compared to untriggered ones. Additional tests can be done by comparing the observed pulse period with the one of the candidate pulsar. Furthermore, to identify events due to Earth occultation of astronomical objects, we can benefit from the position data of the 248 known sources observed with Fermi. With the help of this position data and Fermi's

33

position at the trigger time, we can check if any of these sources come out of the Earth occultation just before the trigger time. If so, we can further check whether triggered detectors see this source with smallest angles compared to untriggered ones. For further check, we can compare the observed flux with the flux history of the candidate source.
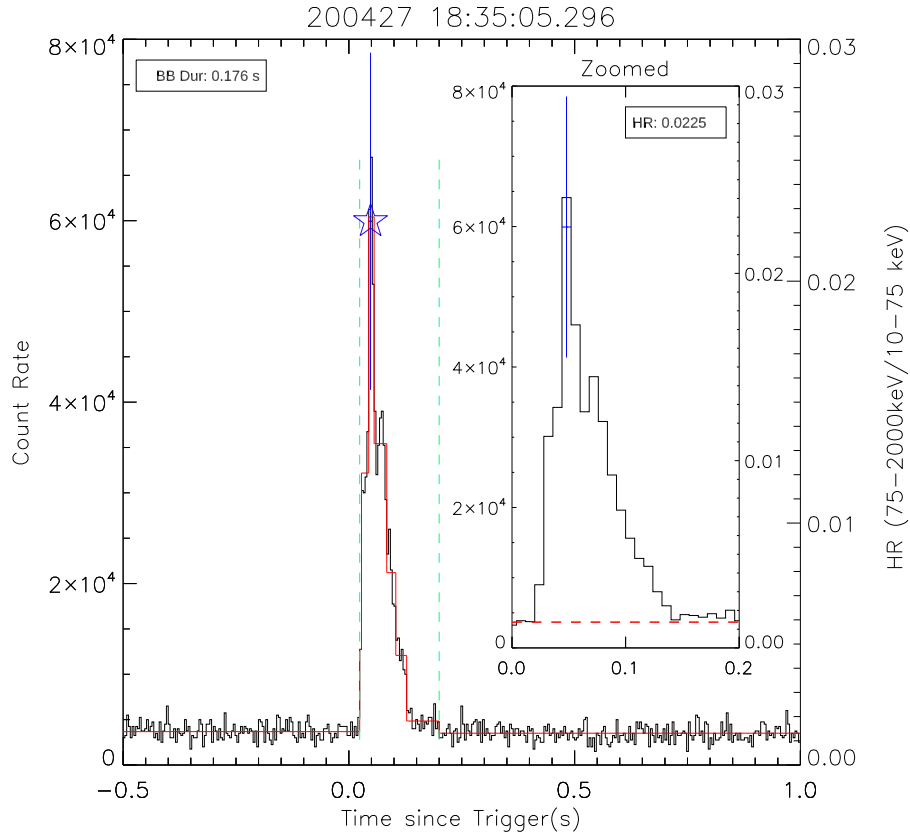

Figure 24 SGR light curve of the brightest 3 "triggered detectors" (n1, n0 & n9) is shown with count rates in the 10-2000 keV range on the left y axis. The red solid lines indicate the BB representation of the light curve. The blue star shows the peak hardness. The green vertical dashed lines show the duration interval. Inside panel zooms into the duration interval and shows the peak hardness value with its error. The red dashed lines show the background level.

To demonstrate how the results of this study could be implemented for identification of an unknown transient event detected with GBM, we present an example here using an event actually found by our untriggered event search. The event was detected with 9 of the NaI(Tl) detectors at 18:35:05 UT on April 27, 2020 in 8 ms time scale and 10-100 keV energy range (see Figure 23). We first performed BB duration analysis and found that the event duration was 0.176 s. Based on the fact that the event is short but not as short as TGFs, we calculated the spectral hardness E_{piv} = 75 keV as 0.0225 (see Figure 24). In addition, we checked the spacecraft L-coordinate (1.22), latitude (-16.3) and longitude (167.6) at the time of trigger, indicating that the spacecraft was at low L-shell value but not at the entrance of SAA. Together with the max-min ratio of 3.66,

we concluded that it should not be a charged particle event. Considering all methods and analyses, we concluded that this should be an SGR burst. From our database, we know that SGR 1935+2154 was active at that time and found that the event in our search matches with the one of SGR 1935+2154 bursts presented in (Lin et al. 2020). Therefore, we checked the angles between the detectors' zenith and the source and found that the brightest 3 detectors (n1, n0 & n9) see the source with the smallest 3 angles ($\sim 30°$).

We have a large sample of unidentified events found under the scope of an ongoing search project. A systematic implementation of the results of this study to the classification at a larger scale has been started.

APPENDIX 1

HR is the ratio of background subtracted hard counts (H^{cnt}) to soft counts (S^{cnt}). Thereby, the error in HR can be estimated as:

$$(1) \qquad \frac{HR_{err}}{HR} = \sqrt{\left(\frac{H^{cnt}_{err}}{H^{cnt}}\right)^2 + \left(\frac{S^{cnt}_{err}}{S^{cnt}}\right)^2}$$

where H^{cnt}_{err} and S^{cnt}_{err} are basically $\sqrt{H^{cnt}}$ and $\sqrt{S^{cnt}}$, respectively.

BIBLIOGRAPHY

Atwood, W.B., et al., 2009, ApJ, 697 1071, doi:10.1088/0004-637X/697/2/1071

Bhat, P.N. et al., 2016, APJ, 223 28, doi: 10.1007/BF00167327

Bloom, J.S., Kulkarni, S.R., Djorgovski, S.G., 2002, APJ 123:1111–1148, doi:10.1086/338893

Bloom, J.S., Prochaska, J.X., Pooley, D., Blake, C.H., Foley, R.J., et al., 2006, ApJ 638:354–368, doi: 10.1086/498107

Briggs, M.S., et al., 2007, AIP Conference Proceedings, 921, 450, doi: 10.1063/1.2757396

Briggs, M.S., et al., 2010, JGR., 115, A07, 323, doi:10.1029/2009JA015242

Briggs, M.S., Xiong, S., Connaughton, V., Tierney, D., Fitzpatrick, G., Foley, S., et al., 2013, JGR Space Physics, 118, 3805–3830, doi:0.1002/jgra.50205

Collazzi, A.C., et al., 2015, ApJ, 778 105, doi: 10.1088/0067-0049/218/1/11

Duncan, R.C., Thompson, C., 1992, ApJ 392:L9–L13, doi:10.1086/186413

Eichler, D., Livio, M., Piran, T. et al., 1989, Nature 340, 126–128, doi:10.1038/340126a0

Fishman, G.J., Bhat, N., Mallozzi, R, Horack, J.M., Koshut, T, Kouveliotou, C., et al., 1994, Science, 264(5163), 1313–6, doi:10.3847/0067-0049/223/2/28

Fishman, G.J., et al., 2011, JGR, 116, A07,304, doi:0.1029/2010JA016084

Fletcher, L. et al., 2011, Space Science Reviews, vol. 159, pp. 19-106, doi:10.1007/s11214-010-9701-8

Fong, W., Berger, E., Chornock, R., Margutti, R., Levan, A.J., et al., 2013, ApJ 769:56, doi:10.1088/0004-637X/769/1/56

Gehrels, N., Cannizzo, J.K., 2012, Phil Trans R Soc A, 371:20120270. doi: 10.1098/rsta.2012.0270

Göğüş, E., et al., 2001, ApJ, 558 228, doi:10.1086/322463

Göğüş, E., et al., 2010, ApJ, 718, 331, doi:10.1088/0004-637X/718/1/331

Gruber, D., et al., 2014, ApJ, 211 12, doi:10.1088/0067-0049/211/1/12

Gurevich, A.V., G. M. Milikh, & R. Roussel-Dupre, 1992, Phys. Lett. A, 165, 463–468, doi:10.1016/0375-9601(92)90348-P

Jenke, P.A. et al., 2016, ApJ, 826, 228, doi:10.3847/0004-637X/826/2/228

Jenke, P.A.et al., 2016, ApJ, 826 37, doi: 10.3847/0004-637X/826/1/37

Kaneko, Y., et al., 2010, ApJ, 710 1335, doi:10.1088/0004-637X/710/2/1335

Kaspi, V.M.& Beloborodov, A., 2017, ARAA, 55:261-301, doi:10.1146/annurev-astro-081915-023329

Kouveliotou, C., Meegan, C., Fishman, G.J., Bhat, N.P., Briggs, M.S., et al., 1993, ApJ 413:L101–L104, doi:10.1086/186969

Kouveliotou, C., Dieters, S., Strohmayer, T. et al., 1998, Nature 393, 235–237, doi:10.1038/30410

Kozlova, A.V., et al., 2016, MNRAS, 460, 2008–2014, doi: 10.1093/mnras/stw1109

Lien, A., et al., 2016, ApJ, 829 7, doi: 10.3847/0004-637X/829/1/7

Lin, L., et al., 2013, ApJ, 778 105, doi: 010.1088/0004-637X/778/2/105

Lin, L., et al., 2020, ApJ, 902 L43, doi: 10.3847/2041-8213/abbefe

MacFadyen, A.I., Woosley, S.E., & Heger, A., 2001, ApJ, 550, 410, doi:10.1086/319698

McIlwain, C.E., 1966, Space Science Reviews, Volume 5, Issue 5, pp.585-598, doi: 10.1007/BF00167327

Meegan, C., Lichti, G., Bhat, P. N., et al., 2009, ApJ, 702,791, doi:10.1088/0004-637X/702/1/791

Mochkovitch, R., Hernanz, M.,Isern, J. et al., 1993, Nature 361, 236–238, doi:10.1038/361236a0

Nakar, E., 2007, Physics Reports, 442:166–236, doi: 10.1016/j.physrep.2007.02.005

Narayan, R., Paczynski, B. & Piran, T., 1992, APJ 395, L83-L86, doi:10.1086/186493

Roberts, O.J., Fitzpatrick, G.,Stanbro, M., McBreen, S., Briggs, M. S., Holzworth, R.H., et al., 2018, JGR SpacePhysics, 123, 4381–4401, doi:10.1029/2017JA024837

Rowlinson, A., O'Brien, P.T., Metzger, B.D., Tanvir, N.R., Levan, 2013, MNRAS. 430, 1061-1087, doi:10.1093/mnras/sts683

Scargle, J.D., et al., 2013, ApJ, 764 167, doi:10.1088/0004-637X/764/2/167

Stanley, M. A., Shao, Xuan-Min, Smith, D. M., Lopez, L. I., Pongratz, M. B., Harlin, J. D., et al., 2006, Geophysical Research Letters, 33, L06803, doi:10.1029/2005GL025537

Thompson, C., Duncan, R.C., 1995, MNRAS 275:255–300, doi:10.1093/mnras/275.2.255

Thompson, C., Duncan, R.C., 1996, ApJ 473:322–342, doi:10.1086/178147

Thompson, T.A., Chang, P. & Quataert, E., 2004, ApJ, 611,380, doi:10.1086/4219699

Wainwright, C., Berger, E. & Penprase, B.E., 2007, ApJ 657:367–377, doi:10.1086/510794

Wilson-Hodge, C.A., et al., 2018, ApJ, 863 9, doi: 10.3847/1538-4357/aace60

Woosley, S.E., 1993, ApJ, 405, 273, doi:10.1086/172359

Woosley, S.E. & Bloom, J.S., 2006, ARAA, 44, 507, doi: 10.1146/annurev.astro.43.072103.150558

von Kienlin, A. et al., 2014, ApJ, 211 13 , doi:10.1088/0067-0049/211/1/13

von Kienlin, A., Meegan, C.A., Paciesas, W.S. et al., 2020, ApJ, 893, 46, doi:10.3847/1538-4357/ab7a18

Zhang, B., 2013, APJ 763, L22, doi:10.1088/2041-8205/763/1/L22